SSRG International Journal of Electrical and Electronics Engineering
ISSN: 2348-8379/ https://doi.org/10.14445/23488379/IJEEE-V13I1P108

Volume 13 Issue 1, 69-94, January 2026

Original Article

Analysis of Torque, Speed, and Power Requirements in Electric Rope Shovel Loading Cycles using Kinematic and Dynamic Models

Junior Rolando Chavez Peralta[1], German Alberto Echaiz Espinoza[2], Carmelo Mayta Ojeda[3],
Fernando Enrique Echaiz Espinoza[4]

[1]*Professional School of Electronic Engineering, Universidad Nacional de San Agustin, Arequipa, Perú.*
[2]*Academic Department of Electronic Engineering, Universidad Nacional de San Agustin, Arequipa, Perú.*
[3]*Academic Department of Physics, Universidad Nacional de San Agustin, Arequipa, Perú.*
[4]*Institute of Mathematics, Federal University of Alagoas, Alagoas, Brazil.*

[1]*Corresponding Author : jchavezper@unsa.edu.pe*

Received: 05 November 2025 Revised: 07 December 2025 Accepted: 06 January 2026 Published: 14 January 2026

Abstract *- This article presents an integrated kinematic and dynamic analysis of the electric rope shovel and the torque, speed, and electrical power demands of the main actuators (swing, hoist, and crowd) during the loading cycle. We combine (i) a 4-degree-of-freedom articulated mechanical model with three rotating joints and one prismatic joint, modeling developed following the steps of the Denavit–Hartenberg methodology; (ii) Newton–Euler dynamic formulation to compute joint torques and link forces; and (iii) processing of field records to parameterize and validate the simulations. MATLAB scripts were used for model implementation, forward kinematics, dynamic simulation, and signal processing of measured motor torque, speed, and power traces. Results show that (a) the developed kinematic and dynamic model is a typical truck loading cycle; (b) regenerative vector-controlled AC drives enable substantial energy regeneration—most notably in swing motion and to a lesser extent in hoist and crowd motions; and (c) differences between simulated and field records of torques are within operational margins during the loading cycle. The results of the simulations, as well as the analysis of energy consumption and regeneration, demonstrate that these tools can facilitate the identification of opportunities to implement improved operational practices, thereby ensuring optimal and safe performance of electric rope shovels. The study contributes (1) the development of a kinematic and dynamic model for electric rope shovels, (2) data analysis and visualization using MATLAB for optimal performance monitoring of the electric rope shovels, and (3) an analysis of energy consumption and regeneration during the truck loading cycle.*

Keywords *- Dynamic modeling, Electric rope shovels, Homogeneous transformation, Kinematic modeling, Variable speed drive.*

1. Introduction

Electric rope shovels are cornerstone equipment for surface mining operations, as they move massive volumes of material and significantly impact the productivity and profitability of mining activities. Optimizing shovel availability and reducing energy costs are therefore high-value objectives for mining operations. Electric rope shovels feature articulated mechanical systems, electric and hydraulic subsystems, and power electronic drives that enable speed and torque control as well as energy regeneration. These performance characteristics vary depending on several factors, such as the level of rock fragmentation and the expertise of the shovel operator.

Despite decades of industrial experience and several significant modeling efforts, two recurring challenges remain: (i) excavation torque is highly stochastic and strongly dependent on geology, blasting quality, and operator technique, which complicates accurate prediction and control; and (ii) although vector-controlled AC drives enable energy regeneration, practical strategies to maximize local reuse of regenerated energy are still underdeveloped and are often evaluated only in isolated case studies.

This study addresses these challenges through the development of a kinematic and dynamic model of a four-degree-of-freedom mechanical system that replicates the motions of an electric rope shovel during a truck loading cycle.

The results of this modeling are compared with field records to (a) estimate the torque of the motors during a typical loading cycle, (b) quantify the energy regenerated by the vector-controlled AC drives, and (c) demonstrate the usefulness of the model for evaluating poor operational practices, deficiencies in rock fragmentation, and conditions affecting the components of the electric rope shovels.

The specific contributions of this article are:

- A clear and reproducible modeling approach is presented, using the Denavit–Hartenberg methodology for forward kinematics and the Newton–Euler method for dynamics, adapted to an electric rope shovel and developed using MATLAB.
- Torque, speed, and power datasets obtained from field records were processed to plot and analyze their behavior during a truck loading cycle. This approach enables comparison and validation of the simulated torque results developed during the loading phase.
- The evaluation of the efficiency of Variable Speed Drives (VSDs) in energy regeneration during the truck loading cycle.
- To demonstrate how the integrated model can be used for fault diagnosis, the identification of best operational practices, efficient energy consumption, and the improvement of equipment lifespan.

Outline: The kinematic and dynamic model is defined in Section 3, and the dynamic torque equations of the swing, hoist, and crowd motions are developed in Section 4; the power stage of electric rope shovels is described in Section 5; the simulated truck loading cycle is developed in Section 6; the analysis of field records and torque simulation is developed in Section 7; and the analysis of the results is developed in Section 8. Finally, Section 9 presents the study's conclusions and proposes directions for future research.

2. State of the Art

This state-of-the-art focuses on three interrelated domains that directly inform the present study: (i) kinematic and dynamic modeling of shovels and excavators, (ii) electrical drive architectures and energy regeneration technologies applicable to electric rope shovels, and (iii) control, operator behaviors, and the challenges of validation with field records. Classical robotics and multibody techniques—specifically Denavit–Hartenberg (DH) kinematic parameterization and Newton–Euler or Lagrangian dynamics—are standard and effective methods for deriving forward and inverse kinematics, as well as for mapping link motions into actuator torques for shovel and excavator mechanisms [1-3].

Application papers have adapted these robotics tools to shovel geometries and cable drum systems, demonstrating that Newton–Euler formulations can reproduce the main torque and tension characteristics observed in instrumented machines when inertial and frictional parameters are carefully identified as described in [4]. Recent multi-loop, multibody studies have reported increased fidelity in predicted link accelerations and reaction loads compared to simplified single-loop models. However, these approaches require more demanding parameter estimation and richer validation datasets, which raise practical challenges for field implementation, as described in [5].

Consequently, Denavit–Hartenberg (DH) and Newton–Euler modeling are appropriate and tractable choices for developing a compact, validated electric rope shovel model, provided that the parameter identification stage (inertia, friction, and payload) utilizes measured cycles and explicitly quantifies uncertainty as described in [1, 4, 5].

Modern electric rope shovels increasingly employ vector-controlled Variable Speed Drives (VSDs) and Active Front Ends (AFEs), which allow bidirectional power flow and enable potential energy regeneration to the DC bus or the external grid, as shown in [6, 7]. Industry reports and technical studies indicate that the realized regeneration fraction depends strongly on duty cycle characteristics (such as the frequency and duration of braking events), DC bus sizing, and the presence of simultaneous motoring loads capable of absorbing regenerated energy, as shown in [6, 8]. Practical impediments to achieving high capture rates include timing mismatches between energy generation and absorption, DC bus overvoltage events, and grid interface protection constraints, as shown in [7, 9]. Consequently, quantitative evaluation of regeneration potential must combine cycle-level torque, speed, and power time series; a drive energy flow model that incorporates DC bus dynamics; and sensitivity analysis with respect to DC link capacity and concurrent load availability as described in [6, 8].

While PI/vector control remains the industrial baseline, research on predictive and optimization-based controllers—such as model predictive control and trajectory optimization—has demonstrated reductions in energy consumption and peak torque in simulation and constrained prototyping environments, as shown in [10]. Empirical studies and operator modeling research also indicate that operator input substantially affects cycle time, the condition of the component, and energy consumption. Moreover, operator assistance and guidance systems have been shown to reduce variability and improve energy metrics in field trials and simulator studies as described in [11, 12]. To draw operationally meaningful conclusions, modeling studies should therefore either incorporate realistic operator profiles obtained from telemetry or evaluate operator assistance strategies through field or high-fidelity simulation experiments that explicitly include energy flows and regeneration effects, as shown in [11, 12].

A recurrent limitation in the literature is the relatively small and narrowly scoped field datasets used for validation; many modeling studies validate their formulations on a limited number of cycles or on synthetic data, which restricts the ability to generalize regeneration estimates and torque prediction accuracy across different rock types, blasting qualities, and operator styles as described in [4, 5, 8]. A small but growing body of research proposes integrated processing chains that extract representative features from telemetry, perform parameter identification, and evaluate energy flows—including regeneration—using drive-level models. However, such pipelines remain uncommon in the open literature and are often limited to single-site case studies as described in [5, 8, 13]. Robust claims regarding regeneration potential and diagnostic utility, therefore, require sufficient cycle count and operational diversity in the validation dataset, reproducible telemetry processing and parameter estimation procedures, and explicit uncertainty quantification (for example, sensitivity to inertia, friction, and payload variation) as described in [5, 8, 13].

The present article identifies and addresses three methodologically precise gaps from the surveyed literature: (1) limited large-scale, data-driven validation of dynamic models—although Newton–Euler and multibody formulations are well established, they are rarely validated across large, heterogeneous telemetry sets that span geological and operational variability, which constrains the models' applicability for fleet-level or site-specific recommendations as described in [4, 5]; (2) scarcity of integrated, systematic energy management studies leveraging local regeneration—while AFE and VSD hardware capabilities are documented, few peer-reviewed studies combine accurate dynamic models, telemetry-driven duty cycles, and DC bus/drive simulations to assess operational strategies for storing, redistributing, or exporting regenerated energy under varied cycle mixes as show in [6, 8]; and (3) a lack of end-to-end demonstrations linking validated dynamic models to operator assistance for increased regeneration-although operator assistance and advanced control concepts have been proposed, there are limited field validated cases in which model outputs were used to design and test operator guidance specifically aimed at improving regeneration capture and reducing peak demand as described in [10, 11].

3. Modeling of the Mechanical System

An electric rope shovel consists of four main mechanical parts: the crawler assembly, the boom assembly, the dipper handle, and the machinery house. Associated with these major mechanical components are four motions performed by an electric rope shovels: the propel motion, which allows the shovel to move, reposition at the working face, or leave blasting areas (this motion is disabled and does not participate during the excavation stage); the swing motion, used to rotate the machinery house; the crowd motion, used to perform truck-loading maneuvers and to load material from the working face by extending or retracting the dipper handle; and finally, the hoist motion, which works in conjunction with the crowd motion to lift the mined material, allowing the operator to position the dipper above the truck for loading during the loading cycle.

An electric rope shovel in the excavation stage can therefore be modeled as an articulated mechanical system with Four Degrees Of Freedom (4DOF), similar to the structure of robotic arms. The modeling process, which involves three rotary joints (swing, boom support, and hoist) and one prismatic joint (crowd), can be performed using established techniques for robotic arms, as proposed in [14, 15].

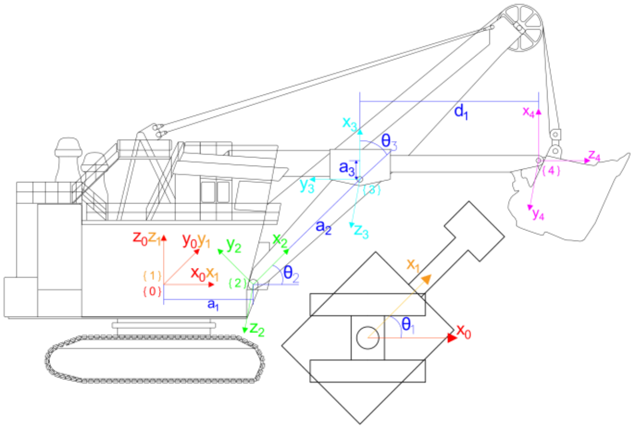

Fig. 1 Link parameters and main joint and assigned frames (Diagram designed in Autodesk AutoCAD 2023)

As described in [14, 15], the mechanical modeling of the electric rope shovels involves both kinematic and dynamic modeling. The kinematic model described the position and orientation of each joint without accounting for the forces involved, whereas the dynamic model defines the forces and torques necessary for motion.

3.1. Kinematics Model of the Electric Rope Shovel

As described in [14-16], the kinematic modeling is performed using forward kinematics by assigning a variable vector to each joint $(\theta_1, \theta_2, \theta_3, d_1)$. This approach defines the final position and orientation of the electric rope shovels. The modeling follows the Denavit–Hartenberg methodology.

3.1.1. Definition of Parameters

The process involves defining the parameters of the joints, where the rotary joints are identified by the angles (θ_i), while the prismatic joints are described in terms of the displacement (d_i). Likewise, the distances between the axes of the rotary joints are expressed in terms of (a_i), as defined in [14, 16].

3.1.2. Assigned to Reference Frames

Once the aforementioned parameters have been established, it is necessary to determine the reference frames for each link of the electric rope shovels, as well as to define the initial reference frame $\{0\}$, as described in [16, 17]. Figure 1 shows the reference frames of each link along with their respective parameters.

3.1.3. Homogeneous Transformations

The description of the position and orientation of the electric rope shovels is achieved by computing the homogeneous transformations between reference frames, which are defined relative to the adjacent reference frames {i+1} and {i}. The combination of these transformations allows the motion of any link to be described with respect to reference frame {0}, as outlined in [14, 15].

The homogeneous transformation matrix is a [4x4] matrix that represents the transformation of a homogeneous coordinate vector from one coordinate system to another, as mentioned in [14-16].

$$T = \begin{bmatrix} R_{3x3} & p_{3x1} \\ f_{1x3} & w_{1x1} \end{bmatrix} = \begin{bmatrix} Rotation & Translation \\ Perspective & Scaling \end{bmatrix} \tag{1}$$

In the present analysis, a zero-perspective transformation and unit global scaling are considered, which implies that the homogeneous transformation (T) is represented by Equation (2).

$$T = \begin{bmatrix} R_{3x3} & p_{3x1} \\ f_{1x3} & w_{1x1} \end{bmatrix} = \begin{bmatrix} Rotation & Translation \\ 0 & 1 \end{bmatrix} \tag{2}$$

In the reference frame (x_1, y_1, z_1), the swing motion is considered, and the corresponding rotation of this joint is described as a rotation about the (z) axis by an angle of (θ_1), with no translation occurring.

Rotation Matrix:

$$ {}^{0}_{1}R = \begin{bmatrix} \cos\theta_1 & -\sin\theta_1 & 0 \\ \sin\theta_1 & \cos\theta_1 & 0 \\ 0 & 0 & 1 \end{bmatrix}$$

Translation Matrix:

$$ {}^{0}_{1}p = \begin{bmatrix} 0 \\ 0 \\ 0 \end{bmatrix}$$

The homogeneous transformation associated with this movement is represented by Equation (3), which is calculated as described in [15].

$$ {}^{0}_{1}T = \begin{bmatrix} \cos\theta_1 & -\sin\theta_1 & 0 & 0 \\ \sin\theta_1 & \cos\theta_1 & 0 & 0 \\ 0 & 0 & 1 & 0 \\ 0 & 0 & 0 & 1 \end{bmatrix} \tag{3}$$

Within the reference frame (x_2, y_2, z_2), the boom support motion can be described by a rotation of (θ_2) about the (y) axis, followed by a 90° rotation about the (x) axis and a translation along the (x) axis of length (a_1).

Rotation matrix:

$$ {}^{1}_{2}R = Roty\ (\theta_2)\ Rotx\ (\pi/2)$$

$$ {}^{1}_{2}R = \begin{bmatrix} \cos\theta_2 & 0 & \sin\theta_2 \\ 0 & 1 & 0 \\ -sin\,\theta_2 & 0 & \cos\theta_2 \end{bmatrix} \begin{bmatrix} 1 & 0 & 0 \\ 0 & cos(\pi/2) & -sin(\pi/2) \\ 0 & sin(\pi/2) & cos(\pi/2) \end{bmatrix}$$

$$ {}^{1}_{2}R = \begin{bmatrix} \cos\theta_2 & 0 & \sin\theta_2 \\ 0 & 1 & 0 \\ -sin\,\theta_2 & 0 & \cos\theta_2 \end{bmatrix} \begin{bmatrix} 1 & 0 & 0 \\ 0 & 0 & -1 \\ 0 & 1 & 0 \end{bmatrix}$$

$$ {}^{1}_{2}R = \begin{bmatrix} \cos\theta_2 & \sin\theta_2 & 0 \\ 0 & 0 & -1 \\ -sin\,\theta_2 & \cos\theta_2 & 0 \end{bmatrix}$$

Translation matrix:

$$ {}^{1}_{2}p = \begin{bmatrix} a_1 \\ 0 \\ 0 \end{bmatrix}$$

Equation (4) illustrates the homogeneous transformation for this motion, following the methodology in [15].

$$ {}^{1}_{2}T = \begin{bmatrix} cos\ \theta_2 & sin\ \theta_2 & 0 & a_1 \\ 0 & 0 & -1 & 0 \\ -sin\ \theta_2 & cos\ \theta_2 & 0 & 0 \\ 0 & 0 & 0 & 1 \end{bmatrix} \tag{4}$$

Considering the reference frame (x_3, y_3, z_3), motion at the saddle block is characterized by a rotation through (θ_3) about the (z) axis, as well as a translation of (a_2) along the (x) axis.

Rotation matrix:

$$ {}^{2}_{3}R = \begin{bmatrix} \cos\theta_3 & -\sin\theta_3 & 0 \\ sin\ \theta_3 & cos\ \theta_3 & 0 \\ 0 & 0 & 1 \end{bmatrix}$$

Translation matrix:

$$ {}^{2}_{3}p = \begin{bmatrix} a_2 \\ 0 \\ 0 \end{bmatrix}$$

As detailed in [15], the homogeneous transformation related to this movement is expressed in Equation (5).

$$ {}^{2}_{3}T = \begin{bmatrix} cos\ \theta_3 & -sin\ \ \theta_3 & 0 & a_2 \\ sin\ \ \theta_3 & cos\ \ \theta_3 & 0 & 0 \\ 0 & 0 & 1 & 0 \\ 0 & 0 & 0 & 1 \end{bmatrix} \tag{5}$$

In the reference frame (x_4, y_4, z_4), the displacement of the dipper handle is considered, which involves a 90° rotation about the (x) axis and a translation along the (x) axis by (a_3), as well as a translation along the (y) axis by (d_1).

Rotation matrix:

$$ {}^{3}_{4}R = \begin{bmatrix} 1 & 0 & 0 \\ 0 & cos(\pi/2) & -sin(\pi/2) \\ 0 & sin(\pi/2) & cos(\pi/2) \end{bmatrix} $$

$$ {}^{3}_{4}R = \begin{bmatrix} 1 & 0 & 0 \\ 0 & 0 & -1 \\ 0 & 1 & 0 \end{bmatrix} $$

Translation matrix:

$$ {}^{3}_{4}p = \begin{bmatrix} a_3 \\ -d_1 \\ 0 \end{bmatrix} $$

The formulation for the homogeneous transformation related to this motion can be found in Equation (6), as expressed in [15].

$$ {}^{3}_{4}T = \begin{bmatrix} 1 & 0 & 0 & a_3 \\ 0 & 0 & -1 & d_1 \\ 0 & 1 & 0 & 0 \\ 0 & 0 & 0 & 1 \end{bmatrix} \tag{6} $$

3.1.4. Simulation of Reference Frames in Three–Dimensional Space

The implementation of the reference frame simulation, based on the previously described homogeneous transformations, relied on the Robotics System Toolbox detailed in [18, 19]. Figure 2 illustrates the three-dimensional reference frames, where frame {0} corresponds to the blue coordinate axis; frame {1}, which describes the swing motion, is represented by the red axis; frame {2}, which describes the motion of the boom support, is shown with the green axis; and frame {3}, representing the hoist motion, is the light blue axis. Finally, frame {4}, which describes the crowd motion, is represented by the pink axis.

3.2. Dynamic Model of the Electric Rope Shovels

The dynamic modeling of an electric rope shovel can be carried out using various methods. Among the most commonly employed are the Newton–Euler equations and the Lagrange formulation, as mentioned by [14, 16].

In the present study, the Newton–Euler equations are used. The objective of dynamic modeling is to establish a clear understanding of the system's behavior. A set of equations that allows the determination of the torques and forces at each joint as a function of the joint variables, taking into account the effects of inertia and gravity.

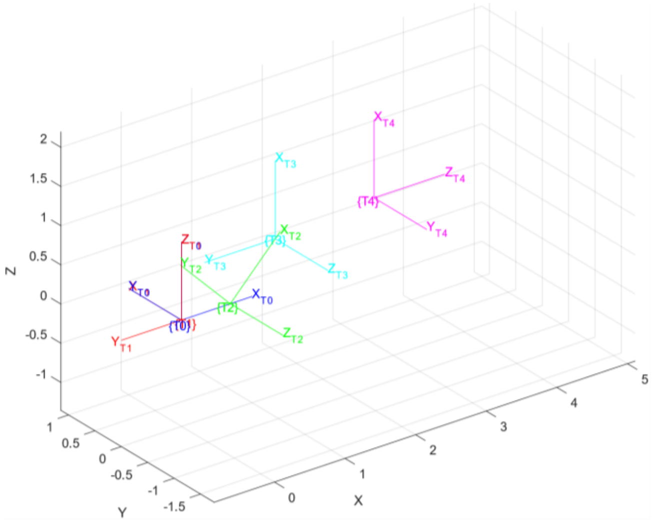

Fig. 2 Representation of homogeneous transforms in a three-dimensional space (Plotted using MATLAB R2025a)

3.2.1. Linear Velocity

The linear velocity, analyzed from the reference frame {i}, is expressed by Equation (7) described in [14, 16].

$$ {}^{i}\mathcal{V}_i = {}^{i}_{i-1}R({}^{i-1}\mathcal{V}_{i-1} + {}^{i-1}\omega_{i-1} \times {}^{i-1}P_i) \tag{7} $$

For i = 1,2,3, which are rotary joints, their linear velocity is given by Equation (8), Equation (9), and Equation (10).

$$ {}^{1}\mathcal{V}_1 = {}^{1}_{0}R({}^{0}\mathcal{V}_0 + {}^{0}\omega_0 \times {}^{0}P_1) \tag{8} $$

$$ {}^{2}\mathcal{V}_2 = {}^{2}_{1}R({}^{1}\mathcal{V}_1 + {}^{1}\omega_1 \times {}^{1}P_2) \tag{9} $$

$$ {}^{3}\mathcal{V}_3 = {}^{3}_{2}R({}^{2}\mathcal{V}_2 + {}^{2}\omega_2 \times {}^{2}P_3) \tag{10} $$

For i = 4, which is a prismatic joint, its linear velocity is given by Equation (11).

$$ {}^{4}\mathcal{V}_4 = {}^{4}_{3}R({}^{3}\mathcal{V}_3 + {}^{3}\omega_3 \times {}^{3}P_4) + \dot{d}_1\,{}^{4}\hat{Z}_4 \tag{11} $$

3.2.2. Angular Velocity

The expression for angular velocity with respect to reference frame {i} is given in Equation (12), as detailed in [14, 16].

$$ {}^{i}\omega_i = {}^{i}_{i-1}R\,{}^{i-1}\omega_{i-1} + \dot{\theta}_i\,{}^{i}\hat{Z}_i \tag{12} $$

For the rotary joints where i = 1,2,3, the angular velocities are provided by Equations (13), (14), and (15).

$$ {}^{1}\omega_1 = {}^{1}_{0}R\,{}^{0}\omega_0 + \dot{\theta}_1\,{}^{1}\hat{Z}_1 \tag{13} $$

$$ {}^{2}\omega_2 = {}^{2}_{1}R\,{}^{1}\omega_1 + \dot{\theta}_2\,{}^{2}\hat{Z}_2 \tag{14} $$

$$ {}^{3}\omega_3 = {}^{3}_{2}R\,{}^{2}\omega_2 + \dot{\theta}_3\,{}^{3}\hat{Z}_3 \tag{15} $$

For i = 4, which is a prismatic joint, its angular velocity is given by Equation (16).

$$ {}^{4}\omega_{4} = {}^{4}_{3}R\,{}^{3}\omega_{3} \tag{16} $$

3.2.3. Linear Acceleration

Equation (17), as detailed in [14, 16], provides the expression for linear acceleration with respect to reference frame {i}.

$$ {}^{i}\dot{\mathcal{V}}_{i} = {}^{i}_{i-1}R[\,{}^{i-1}\dot{\mathcal{V}}_{i-1} + {}^{i-1}\omega_{i-1} \times {}^{i-1}P_{i} + {}^{i-1}\omega_{i-1} \times (\,{}^{i-1}\omega_{i-1} \times {}^{i-1}P_{i})] \tag{17} $$

The linear acceleration for each rotary joint i = 1,2,3 is determined by Equations (18), (19), and (20).

$$ {}^{1}\dot{\mathcal{V}}_{1} = {}^{1}_{0}R\left[\,{}^{0}\dot{\mathcal{V}}_{0} + {}^{0}\omega_{0} \times {}^{0}P_{1} + {}^{0}\omega_{0} \times (\,{}^{0}\omega_{0} \times {}^{0}P_{1})\right] \tag{18} $$

$$ {}^{2}\dot{\mathcal{V}}_{2} = {}^{2}_{1}R\left[\,{}^{1}\dot{\mathcal{V}}_{1} + {}^{1}\omega_{1} \times {}^{1}P_{2} + {}^{1}\omega_{1} \times (\,{}^{1}\omega_{1} \times {}^{1}P_{2i})\right] \tag{19} $$

$$ {}^{3}\dot{\mathcal{V}}_{3} = {}^{3}_{2}R\left[\,{}^{2}\dot{\mathcal{V}}_{2} + {}^{2}\omega_{2} \times {}^{2}P_{3} + {}^{2}\omega_{2} \times (\,{}^{2}\omega_{2} \times {}^{2}P_{3})\right] \tag{20} $$

For i = 4, which is a prismatic joint, its linear acceleration is given by Equation (21).

$$ {}^{4}\dot{\mathcal{V}}_{4} = {}^{4}_{3}R\left[\,{}^{3}\dot{\mathcal{V}}_{3} + {}^{3}\dot{\omega}_{3} \times {}^{3}P_{4} + {}^{3}\omega_{3} \times (\,{}^{3}\omega_{3} \times {}^{3}P_{4})\right] + 2\,{}^{3}\omega_{3} \times \dot{d}_{1}\,{}^{4}\hat{Z}_{4} + \ddot{d}_{1}\,{}^{4}\hat{Z}_{4} \tag{21} $$

3.2.4. Angular Acceleration

As described in [14, 16], the linear acceleration in reference frame {i} is given by Equation (22).

$$ {}^{i}\dot{\omega}_{i} = {}^{i}_{i-1}R\,{}^{i-1}\dot{\omega}_{i-1} + {}^{i}_{i-1}R\,{}^{i-1}\omega_{i-1} \times \dot{\theta}_{i}\,{}^{i}\hat{Z}_{i} + \ddot{\theta}_{i}\,{}^{i}\hat{Z}_{i} \tag{22} $$

Equations (23), (24), and (25) detail the angular acceleration to the rotary joints, i = 1,2,3.

$$ {}^{1}\dot{\omega}_{1} = {}^{1}_{0}R\,{}^{0}\dot{\omega}_{0} + {}^{1}_{0}R\,{}^{0}\omega_{0} \times \dot{\theta}_{1}\,{}^{1}\hat{Z}_{1} + \ddot{\theta}_{1}\,{}^{1}\hat{Z}_{1} \tag{23} $$

$$ {}^{2}\dot{\omega}_{2} = {}^{2}_{1}R\,{}^{1}\dot{\omega}_{1} + {}^{2}_{1}R\,{}^{1}\omega_{1} \times \dot{\theta}_{2}\,{}^{2}\hat{Z}_{2} + \ddot{\theta}_{2}\,{}^{2}\hat{Z}_{2} \tag{24} $$

$$ {}^{3}\dot{\omega}_{3} = {}^{3}_{2}R\,{}^{2}\dot{\omega}_{2} + {}^{3}_{2}R\,{}^{2}\omega_{2} \times \dot{\theta}_{3}\,{}^{3}\hat{Z}_{3} + \ddot{\theta}_{3}\,{}^{3}\hat{Z}_{3} \tag{25} $$

For i = 4, which is a prismatic joint, its angular acceleration is given by equation (26).

$$ {}^{4}\dot{\omega}_{4} = {}^{4}_{3}R\,{}^{3}\dot{\omega}_{3} \tag{26} $$

3.2.5. Forces

The force on the link for a reference frame {i} is expressed by Equation (27), as described in [14, 16].

$$ {}^{i}F_{i} = m_{i}\,{}^{i}\dot{v}_{c_{i}} \tag{27} $$

As for the rotary joints i = 1,2,3, their respective angular velocities are described by Equation (28), Equation (29), and Equation (30).

$$ {}^{1}F_{1} = m_{1}\,{}^{1}\dot{v}_{c_{1}} \tag{28} $$

$$ {}^{2}F_{2} = m_{2}\,{}^{2}\dot{v}_{c_{2}} \tag{29} $$

$$ {}^{3}F_{3} = m_{3}\,{}^{3}\dot{v}_{c_{3}} \tag{30} $$

For i = 4, the analysis will be divided into two sections: one section will focus on obtaining the forces for the dipper handle in {4.1}, and the other section will focus on the forces for the dipper in {4.2}, as described in [16]. The corresponding forces are Equation (31) and Equation (32).

$$ {}^{4}F_{4.1} = m_{4.1}\,{}^{4}\dot{v}_{c_{4.1}} \tag{31} $$

$$ {}^{4}F_{4.2} = \left(m_{4.1} + m_{carga}\right)\,{}^{4}\dot{v}_{c_{4.2}} \tag{32} $$

3.2.6. Torsion Moments

The moment of force corresponding to each link in a reference frame {i} is expressed by Equation (33) described in [14, 16].

$$ {}^{i}N_{i} = {}^{c_{i}}I\,{}^{i}\dot{\omega}_{i} + {}^{i}\omega_{i} \times {}^{c_{i}}I\,{}^{i}\omega_{i} \tag{33} $$

Equations (34), (35), and (36) detail the torsion moments corresponding to the rotary joints, i = 1,2,3.

$$ {}^{1}N_{1} = {}^{c_{1}}I\,{}^{1}\dot{\omega}_{1} + {}^{1}\omega_{1} \times {}^{c_{1}}I\,{}^{1}\omega_{1} \tag{34} $$

$$ {}^{2}N_{2} = {}^{c_{2}}I\,{}^{2}\dot{\omega}_{2} + {}^{2}\omega_{2} \times {}^{c_{2}}I\,{}^{2}\omega_{2} \tag{35} $$

$$ {}^{3}N_{3} = {}^{c_{3}}I\,{}^{3}\dot{\omega}_{3} + {}^{3}\omega_{3} \times {}^{c_{3}}I\,{}^{3}\omega_{3} \tag{36} $$

For i = 4, the analysis is divided into two sections with the objective of determining the torque individually: for the dipper handle, the frame of reference is {4.1}, and for the dipper, the frame of reference is {4.2}, as described in [16]. The corresponding torsion moments are Equations (37) and (38).

$$ {}^{4}N_{4.1} = {}^{c_{4.1}}I\,{}^{4}\dot{\omega}_{4} + {}^{4}\omega_{4} \times {}^{c_{4.1}}I\,{}^{4}\omega_{4} \tag{37} $$

$$ {}^{4}N_{4.2} = {}^{c_{4.2}}I\,{}^{4}\dot{\omega}_{4} + {}^{4}\omega_{4} \times {}^{c_{4.2}}I\,{}^{4}\omega_{4} \tag{38} $$

After determining the forces and moments on each link, the torque moments at the joints must be calculated. These moments arise from the application of the net forces and moments on each of the links. The net force on the link for a reference frame {i} is expressed by Equation (39) according to [14, 16].

$$ {}^{i}f_i = {}^{i}F_i + {}^{i}_{i+1}R\,{}^{i+1}f_{i+1} \tag{39}$$

For i = 1,2,3, which are frames with rotary joints, their net force is given by Equations (40), (41), and (42).

$$ {}^{1}f_1 = {}^{1}F_1 + {}^{1}_{2}R\,{}^{2}f_2 \tag{40}$$

$$ {}^{2}f_2 = {}^{2}F_2 + {}^{2}_{3}R\,{}^{3}f_3 \tag{41}$$

$$ {}^{3}f_3 = {}^{3}F_3 + {}^{3}_{4}R\,{}^{4}f_4 \tag{42}$$

For i = 4, which is a prismatic joint, their net force is given by Equation (43).

$$ {}^{4}f_4 = {}^{4}F_{4.1} + {}^{4}F_{4.2} \tag{43}$$

The torsion moment on the link for a reference frame {i} is expressed by Equation (44) as presented in [14, 16].

$$ {}^{i}n_i = {}^{i}N_i + {}^{i}_{i+1}R\,{}^{i+1}n_{i+1} + {}^{i}P_{c_i} \times {}^{i}F_i + {}^{i}P_{i+1} \times {}^{i}_{i+1}R\,{}^{i+1}f_{i+1} \tag{44}$$

For i = 1,2,3, which are frames with rotary joints, their torsion moment is given by Equations (45), (46), and (47).

$$ {}^{1}n_1 = {}^{1}N_1 + {}^{1}_{2}R\,{}^{2}n_2 + {}^{1}P_{c_1} \times {}^{1}F_1 + {}^{1}P_2 \times {}^{1}_{2}R\,{}^{2}f_2 \tag{45}$$

$$ {}^{2}n_2 = {}^{2}N_2 + {}^{2}_{3}R\,{}^{3}n_3 + {}^{2}P_{c_2} \times {}^{2}F_2 + {}^{2}P_3 \times {}^{2}_{3}R\,{}^{3}f_3 \tag{46}$$

$$ {}^{3}n_3 = {}^{3}N_3 + {}^{3}_{4}R\,{}^{4}n_4 + {}^{3}P_{c_3} \times {}^{3}F_3 + {}^{3}P_4 \times {}^{3}_{4}R\,{}^{4}f_4 \tag{47}$$

For i = 4, which is a prismatic joint, their torsion moment is given by Equation (48).

$$ {}^{4}n_4 = {}^{4}N_4 + {}^{4}P_{c_4} \times {}^{4}F_4 + {}^{4}N_4 + {}^{4}P_{c_4} \times {}^{4}F_4 \tag{48}$$

Therefore, to find the torque required at each joint to maintain static equilibrium according to [14, 16] the dot product of the joint axis vector with the moment vector acting on the link is calculated; the joints only produce torsion moments and forces in the Z axis; and the resulting torques are given by Equations (49), (50), (51), and (52).

$$ \tau_1 = {}^{1}n_1{}^{T}[0 \quad 0 \quad 1]^{T} \tag{49}$$

$$ \tau_2 = {}^{2}n_2{}^{T}[0 \quad 0 \quad 1]^{T} \tag{50}$$

$$ \tau_3 = {}^{3}n_3{}^{T}[0 \quad 0 \quad 1]^{T} \tag{51}$$

$$ \tau_4 = {}^{4}f_4{}^{T}[0 \quad 0 \quad 1]^{T} \tag{52}$$

3.3. Centers of Mass and Inertia Tensors

As detailed in [14, 16], for a rigid body that can move in three dimensions, there are infinitely many possible axes of rotation. In the case of rotation about an arbitrary axis, a complex method is required to characterize the mass distribution of a rigid body. The centers of mass and moments of inertia of the electric rope shovels' links were calculated using simplified models of the revolving frame, boom, dipper handle, and bucket. The calculations are performed using simulations in MATLAB and Autodesk Inventor, obtaining estimates of the center of mass and moment of inertia of the electric shovel components.

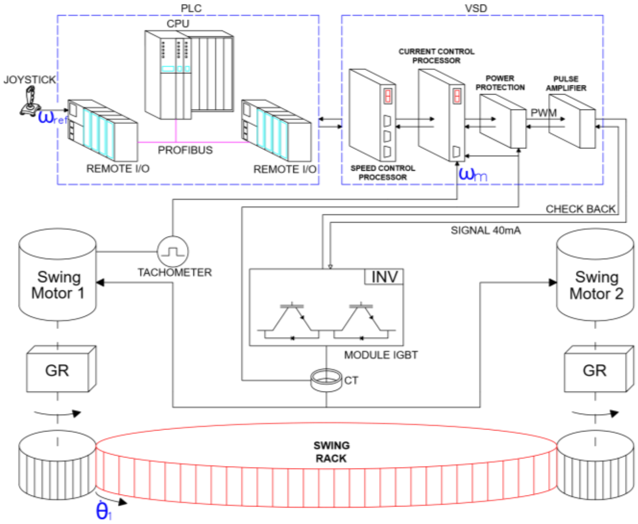

Fig. 3 Drive arrangement for swing motion (adapted from [16]) (Diagram designed in AutoCAD)

4. Determination of Motor Torques

Once the equations for calculating the torques of each link of the electric rope shovels were obtained, the next step was to determine the torques that the hoist, crowd, and swing motors must develop to produce the required movements during the loading cycle. Subsequently, a set of data was obtained and used to compare with the torques developed in field records.

4.1. Swing Motor

The swing system consists of two electric motors mounted vertically on a planetary gearbox, located on the left and right sides of the swing rack. Each motor is equipped with its own fan and drives the planetary gear system through a coupling. The disc brake system, spring-applied and released by an air relief mechanism, sits on top of the swing motors. Each gearbox has its own lubrication pump that is powered by a motor. This pump sends oil to the important parts of the gearbox. These gears transmit torque to a pair of pinions positioned at the lower end of the shaft, which engage with the swing rack.

As shown in Figure 3, both motors are powered by a single inverter with vector control, distributing the required power evenly between them. A single tachometer indicates the speed of both motors. The Variable Speed Drive (VSD) sends and receives control signals from the inverter, the tachometer, and the current transducer. The speed reference is provided by the joystick signal, which is sent to the Programmable Logic Controller (PLC) that directly interacts with the VSD to control the swing speed of the electric rope shovels. Consequently, the dynamic equation corresponding to the swing motors is expressed by Equation (53), as described in [16].

$$T_{em1} + T_{em2} = b_s\omega_{ms} + 2J_{mots}\frac{d\omega_{ms}}{dt} + \left(\frac{1}{n_{gr1}}\right)$$

$$\tau_1(\Theta, \dot{\Theta}, \ddot{\Theta}, m_{carga}) + T_{digg.s} \tag{53}$$

The terms appearing in Equation (53) are defined as follows:

- $T_{em1} + T_{em2}$ this term denotes the sum of the torques developed by the two electric swing motors.
- $b_s\omega_{ms}$ represents the torque generated by friction, where b_s is the friction coefficient and ω_{ms} is the angular speed of the swing motor.
- $2J_{mots}\frac{d\omega_{ms}}{dt}$ corresponds to the torque resulting from the combined inertia of both motors, where J_{mots} is the motor inertia.
- $\frac{1}{n_{gr1}}$ indicates the reduction factor of the gear system.
- $\tau_1(\Theta, \dot{\Theta}, \ddot{\Theta}, m_{carga})$ refers to the torque obtained from the dynamic modelling.
- $T_{digg.s}$ denotes the additional torque required due to material resistance during the excavation stage.

4.2. Hoist Motor

The hoist system consists of a planetary gearbox that drives a pair of pinions. These pinions generate the hoist drum's rotation, enabling the winding or unwinding of the hoist cables, which allows the bucket to move up or down. The gearbox is coupled to the electric motor through a shaft. When the operator moves the joystick, it sends a signal to the Programmable Logic Controller (PLC) to control the hoist motor via the Variable Speed Drive (VSD). This system operates in conjunction with the crowd system. The hoist motor is powered by two vector-controlled inverters, with continuous monitoring of temperature, voltage, speed, and current, thereby regulating the torque–speed ratio required for proper operation.

As shown in Figure 4, the force (F_H) value varies with the position of the saddle block, represented by the variation of the angle (δ_1). Consequently, the required driving torque depends not only on the load but also on the dynamic position of the saddle block and other operational parameters.

To derive the dynamic equation for the hoist motor, the torques generated at the hoist drum are compared with the torque required to move the bucket. The calculations are performed under ideal conditions; therefore, the force needed at the hoist drum to wind the cables is equivalent to the force required to raise or lower the bucket. Based on this relationship, the dynamic torque (τ_2') is determined and is expressed by Equation (56). Then, based on the torque produced by the hoist drum, the force (F_H) is determined and is expressed by Equation (54).

$$\tau_2' = F_H r_{HD} \sin 90$$

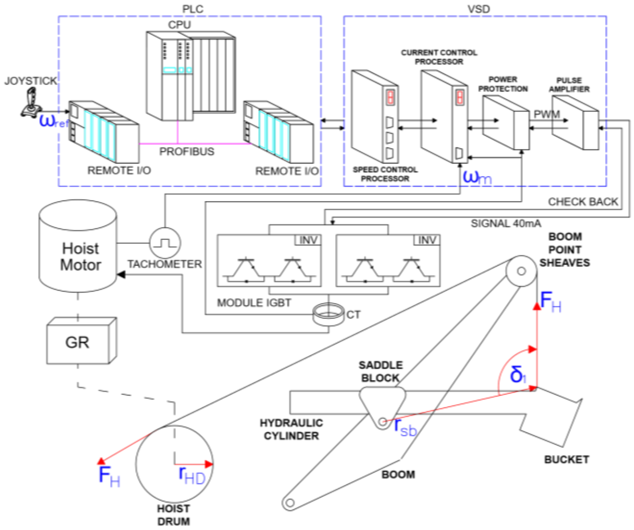

Fig. 4 Drive arrangement for hoist motion (adapted from [16]) (Diagram designed in Autodesk AutoCAD 2023)

$$F_H = \frac{\tau_2'}{r_{HD}} \tag{54}$$

and

$$\tau_2 = F_H r_{sb} \sin \delta_1 \tag{55}$$

By substituting the force (F_H) into Equation (55), the relationship between the torque of the hoist drum and the torque of the bucket is established. This relationship is expressed in Equation (56).

$$\tau_2 = \frac{\tau_2' r_{sb} \sin \delta_1}{r_{HD}}$$

$$\tau_2' = \frac{r_{HD}}{r_{sb} \sin \delta_1}\tau_2 \tag{56}$$

The terms used in Equation (56) are specified as follows:

- F_H denotes the force exerted by the hoist drum when winding the hoist cables.
- r_{HD} represents the hoist drum radius.
- r_{sb} corresponds to the distance between the axis of the saddle block and the bucket.
- δ_1 indicates the angle formed with respect to the position and orientation of the dipper handle.

As a result, the dynamic equation for the hoist motor is given by Equation (57), as detailed in [16].

$$\begin{aligned} T_{emH} = b_H\omega_{mH} + J_{motH}\frac{d\omega_{mH}}{dt} + \left(\frac{1}{n_{gr2}}\right) \\ \tau_2{}'(\Theta,\dot{\Theta},\ddot{\Theta},m_{carga}) + T_{digg} \end{aligned} \qquad (57)$$

The variables in Equation (57) are defined as follows:

- T_{emH} represents the torque developed by the hoist motor.
- $b_H\omega_{mH}$ represents the torque generated by friction, where b_H is the friction coefficient and ω_{mH} is the angular speed of the hoist motor.
- $J_{motH}\frac{d\omega_{mH}}{dt}$ correspond to the torque resulting from the inertia of the motor, where J_{motH} is the motor inertia.
- $\frac{1}{n_{gr2}}$ indicates the reduction factor of the gear system.
- $\tau_2{}'(\Theta,\dot{\Theta},\ddot{\Theta},m_{carga})$ refers to the torque obtained from the dynamic modelling.
- T_{digg} denotes the additional torque required due to material resistance during the excavation stage.

4.3. Crowd Motor

The crowd motion is used in conjunction with the hoist motion during the excavation phase. The force required for the movement of the dipper handle is transmitted through a hydraulic cylinder, which performs the extension and retraction. This process is regulated by a valve block that receives hydraulic oil supplied via the pump control block. The pump transmission is coupled to an electric motor.

The crowd motor is powered by a vector-controlled inverter, with continuous monitoring of its speed and current, thereby regulating the torque–speed ratio required for its operation.

As shown in Figure 5, the force (F_{Crowd}) applied by the hydraulic cylinder during retraction and extension is counteracted by a component ($F_H\cos\alpha_1$) of the force (F_H). This component varies in magnitude according to the changes in the angles (δ_1) and (α_1). Based on the methodology described in [16, 17, 20], the torque ($\tau_3{}'$) is formulated as expressed in Equation (58).

$$\tau_3{}' = (F_{Crowd} - F_H\cos\alpha_1)r_{SD} + \tau_3 \qquad (58)$$

The variables in Equation (58) are defined as follows:

- F_{Crowd} represents the force generated by the hydraulic cylinder.
- F_H denotes the force exerted by the hoist drum when winding the hoist cables.

As a result, the dynamic equation for the crowd motor is given by (59).

$$\begin{aligned} T_{emC} = b_C\omega_{mC} + J_{motC}\frac{d\omega_{mC}}{dt} + \tau_3{}'(\Theta,\dot{\Theta},\ddot{\Theta},m_{carga}) \\ +T_{digg} \end{aligned} \qquad (59)$$

The variables in Equation (57) are defined as follows:

- T_{emC} represents the torque developed by the crowd.
- $b_C\omega_{mC}$ represents the torque generated by friction, where b_H is the friction coefficient and ω_{mH} is the angular speed of the crowd motor.

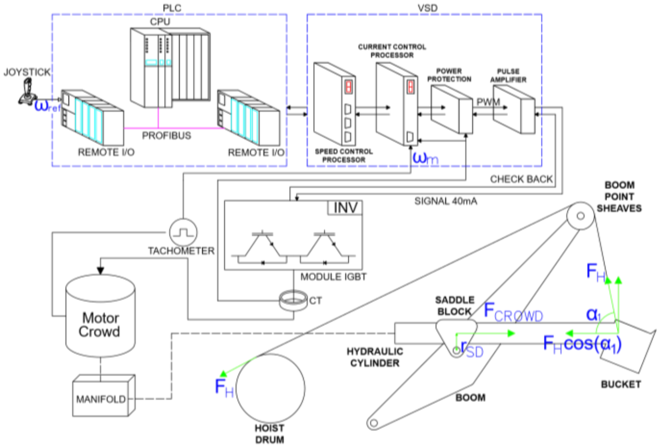

Fig. 5 Drive arrangement for crowd motion (adapted from [16]) (Diagram designed in Autodesk AutoCAD 2023)

- $J_{motC}\frac{d\omega_{mC}}{dt}$ correspond to the torque resulting from the inertia of the motor, where J_{motH} is the inertia of the motor.
- $\tau_3{}'(\Theta,\dot{\Theta},\ddot{\Theta},m_{carga})$ refers to the torque obtained from the dynamic modelling.
- T_{digg} denotes the additional torque required due to material resistance during the excavation stage.

5. Active Front-End and Vector-Controlled AC Drives

Unlike traditional passive rectifiers based on diodes or thyristors, Active Front Ends (AFEs) employ fully controlled PWM converters, which are typically composed of IGBTs or MOSFETs. This configuration allows operation in both motoring and regeneration modes. In conventional operation, the AFE converts the AC grid voltage into a regulated, lowdistortion DC voltage, maintaining the DC bus within the required limits to supply an inverter that controls electric motors.

The main uses for Variable Speed Drives (VSD) are to control the speed and torque of electric motors. Electric rope shovels, electric drills, conveyor belts, electric trucks, and mills are some of the mining industry equipment that use these kinds of controllers.

These controllers can do many things, such as controlling the starting current, adjusting for reactive power, maintaining a steady power factor, recovering energy, protecting against sudden spikes in current, and connecting to other devices like Human-Machine Interfaces (HMIs), Programmable Logic Controllers (PLCs), and other variable speed drives.

5.1. Stages of the Variable Speed Drive

The stages of the electric rope shovel’s variable speed drive are illustrated in Figure 6, and they are divided into the following three stages:

5.1.1. Rectification Stage

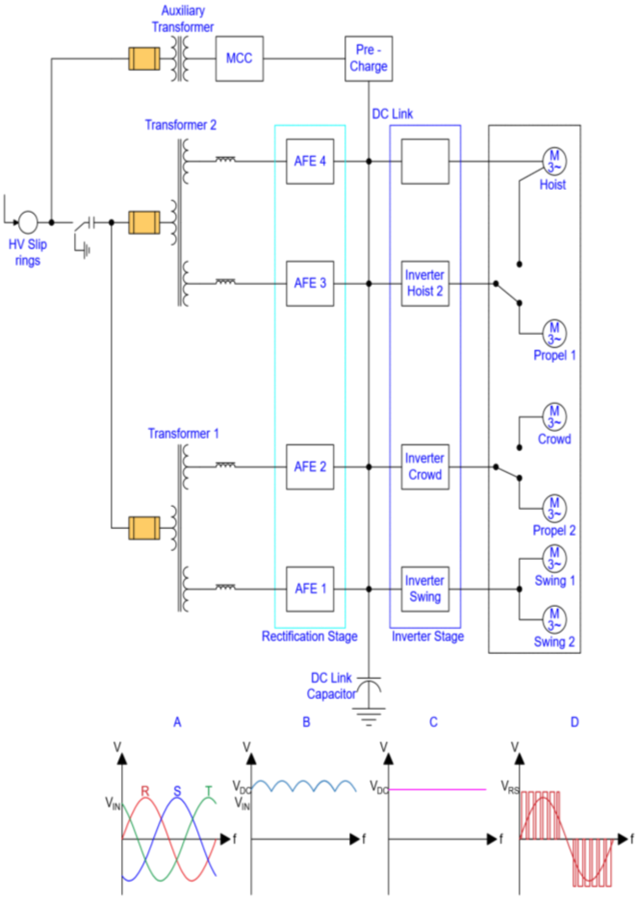

Fig. 6 Regenerative shovel drive system (a) Three-phase voltage, (b) The rectified voltage, (c) Stabilized DC voltage, and (d) PWM signal (adapted from [22]) (Diagram designed in Autodesk AutoCAD 2023).

Rectification is the first phase of the power stage in an electric system, as shown in Figure 6. This stage is responsible for converting the AC energy supplied by the grid, via the HV slip rings, into regulated DC energy. The voltage provided by the main transformers (Transformer 1 and Transformer 2) supplies the four Active Front-End (AFE) modules, designated as AFE 1, AFE 2, AFE 3, and AFE 4.

Each AFE operates as a controlled rectifier with bidirectional capability, allowing not only AC–DC conversion but also the return of regenerated energy from the motors back to the grid. These active rectifiers minimize current harmonic content, maintain a power factor close to unity, and regulate the DC bus voltage. In Figure 6, the lower part shows (a) the waveform of the three-phase AC voltage and (b) the rectified voltage.

5.1.2. DC Link

The voltage rectified by the AFEs is stored in the DC link, which behaves as a transfer node between the rectification and inversion stages. The DC link consists of a passive filter composed of a capacitor bank, which stabilizes the DC voltage and supplies instantaneous energy to the inverters during high-demand conditions. The voltage level of the DC link is regulated by the control of the AFEs, ensuring that the inverters operate under stable conditions. In the lower part of Figure 6, (c) represents the stabilized DC bus voltage, which is ready to be processed by the inverters.

5.1.3. Inverter Stage

In the final power stage, the inverters are responsible for converting the DC bus voltage into AC voltage to drive the main motors of the electric rope shovels. Each inverter employs PWM modulation and vector control to determine the three-phase voltages and currents required to regulate the torque and speed for the hoist, crowd, swing, and propel motions. When these motors operate as generators, they return energy to the DC link, which can be utilized by another inverter or processed by the AFEs and fed back to the electrical grid. In the lower part of Figure 6, (d) shows the PWM waveform produced by the inverters, illustrating the conversion of DC voltage into a modulated AC signal suitable for the three-phase motors.

5.2. AFEs and Regenerative Energy

During the truck loading cycle, several motors (hoist, swing, and crowd) of an electric rope shovel operate alternately, either consuming or regenerating energy. When these motors function as generators, the kinetic or potential energy of the mechanical system is converted back into electrical energy, which flows to the inverters and is directed to the DC link, where it is temporarily stored in the bus capacitors.

From there, the regenerated energy can be reused by other inverters or processed by the AFEs, which allow this energy to be returned to the electrical grid in a synchronized manner. As shown in Figure 6, this process is sampled by the bidirectional system between the motors, inverters, and AFEs, enabling the utilization of energy generated during deceleration, braking, or load lowering. Energy regeneration significantly contributes to reducing the net energy consumed during the loading cycle, thereby improving the efficiency of an electric shovel. This principle is described in [21, 22].

5.3. Control Diagram Definition for Electric Rope Shovel Motions

The Variable Speed Drive (VSD) controls the speed and torque of an induction motor by simultaneously adjusting the voltage and frequency supplied to it, maintaining a constant V/f ratio. This is to keep the motor's magnetic flux (ϕ) within appropriate levels. If the frequency decreases, the VSD reduces the voltage to prevent core saturation; conversely, if the frequency increases, the VSD raises the voltage to avoid torque loss. In the following paragraph, any reference made to control blocks corresponds directly to those illustrated in Figure 7. This figure provides a detailed schematic of the control system for the swing, crowd, and hoist motions. The frequency and voltage command are determined through a sequence of control stages. Initially, the speed command (1), this signal comes from the reference the operator gives to the joysticks; this signal is sent to the Programmable Logic Controller (PLC), and is transmitted to the ramp generator (2), which is configured according to the operational characteristics of the electric rope shovels.

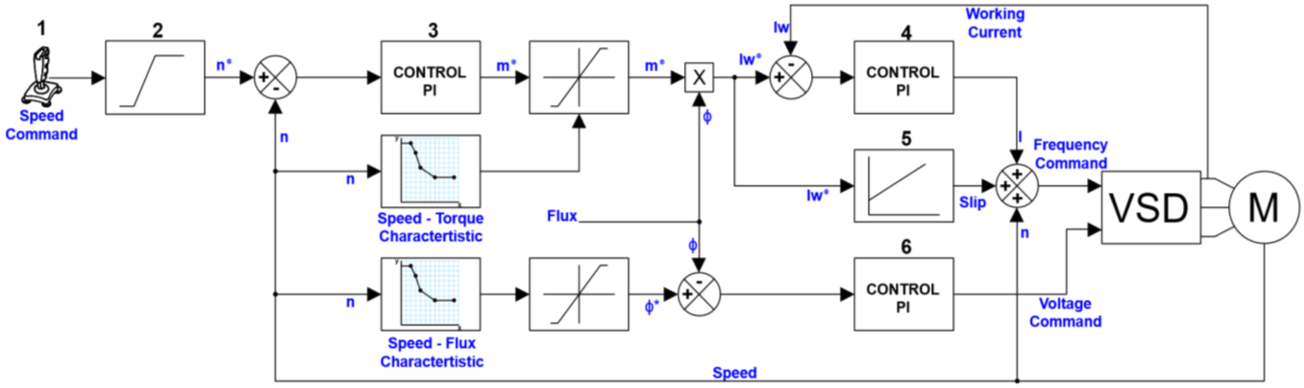

Fig. 7 Control diagram of the hoist, swing, and crowd (Diagram designed in Autodesk AutoCAD 2023)

This block outputs the reference speed (n*). Then the actual speed (n), measured by the tachometer, is compared with the reference speed (n*); a Proportional–Integral (PI) control is applied to the speed error signal; and the magnitude and direction of the torque (m*) to be applied with respect to the reference speed are obtained. The resulting torque (m*) is evaluated against the characteristic speed–torque limits to ensure that it remains within the system's operational parameters.

The calculated torque (m*) is then multiplied by the flux to determine the rotor current (l_w^*), which is required to generate the desired torque. Block (5) calculates the slip necessary to produce a current equal to (l_w^*), while block (4) compares the actual working current (Iw) with the reference working current (l_w^*). Finally, the frequency command supplied to the motor is obtained by summing the outputs from the slip block, the current regulator, and the actual speed measured by the tachometer.

To generate the voltage command, the reference flux is first calculated according to the flux–speed characteristics of the system. The actual flux is then compared to the reference value, and the resulting flux error is processed by block (6); a Proportional–Integral (PI) control is applied to the flux error, and the regulator's output establishes the voltage command. This command serves as the reference for the PWM controller, which ultimately determines the effective voltage supplied to the motor.

6. Simulation of a Truck Loading Cycle

To evaluate a complete loading cycle of a mining electric rope shovel, the equations derived from kinematic and dynamic modeling are essential, as they describe the shovel's motions during the loading phase. The loading cycle is defined by the motions performed by the shovel, all of which are driven by electric motors. Therefore, analysis of the most relevant mechanical and electrical variables is required.

6.1. Shovel Drive References

The loading cycle of an electric rope shovel begins once the operator has dispatched the truck with its full load, and the shovel is positioned at a 90° angle from the working face. Figure 8 provides a detailed description of the motions performed by the electric rope shovel during a loading cycle. Initially, the operator sets a negative reference on the swing joystick until reaching its maximum value, positioning the bucket in front of the working area.

The swing motion, represented by the blue signal, follows the corresponding instruction, displaying a descending acceleration ramp until reaching the maximum operating speed, followed by an ascending deceleration ramp that leads to a complete stop, as shown by the blue curve in Figure 8. At t=13 s, the bucket reaches the working face, where the swing motion remains at zero speed until the loading process is completed at t=24 s. At this point, the operator moves it again in the swing motion toward the truck.

When analyzing the references for the hoist and crowd motors during the initial period of the swing motion, both motors remain stopped, as shown in Figure 8, as their speed commands are set to zero. Once the bucket approaches the central position, the hoist motor begins lowering the bucket, while the crowd motor retracts the dipper handle to close the bucket gate and position it for the start of the excavation process. This sequence is illustrated by the red and green curves in Figure 8 during the time interval from 8 to 13 s.

During the excavation phase, between 13 and 24 s, the operator initially adjusts the hoist joystick to a low reference value to gradually lift the bucket. The crowd joystick is moved to its maximum reference for excavation while the bucket is in the working position, within a 14-16 s interval.

Next, the crowd reference is reduced, and the hoist reference is increased, following an upward trajectory as the bucket fills. At the end of the excavation, the operator briefly applies a negative reference to the crowd motor to separate the bucket from the working face. Subsequently, the bucket is positioned to execute the swing motion toward the truck location, completing the loading sequence.

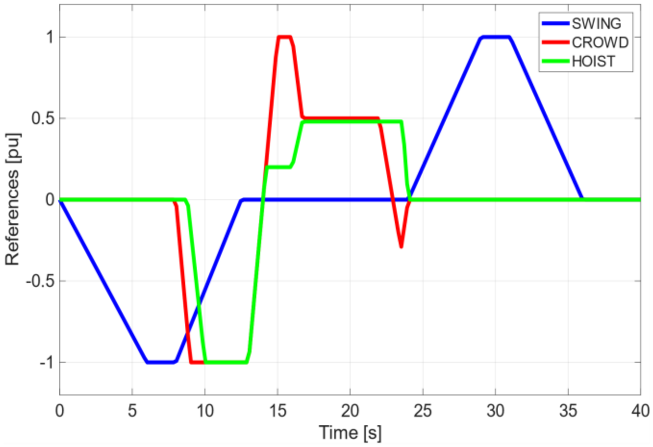

Fig. 8 Idealized shovel drive references (adapted from [3]) (Plotted using MATLAB R2025a)

6.2. Joint Variables

The motions performed by the operator during a loading cycle are proportional to the variations in the angular rotation of the swing and hoist joints, represented by the angles (θ_1) and (θ_3), as well as the displacement of the dipper handle, denoted by the variable (d_1).

By means of the previously described kinematic modeling, it is possible to simulate the behavior of the variations in angles (θ_1), (θ_3), and the displacement (d_1). This simulation allows for a detailed analysis of how these parameters evolve throughout the truck loading cycle. The swing drive mechanism produces the rotation of the electric rope shovel's machinery house, covering an angle from 90° to 0° as the shovel moves from the truck loading position to the center of the working area. Once the bucket is fully loaded, a subsequent rotation occurs, spanning from 0° to 90°; the variation of the (θ_1) angle is shown in Figure 9.

Figure 10 illustrates the variation of angle (θ_3), while Figure 11 samples the displacement (d_1) during the loading cycle. In this context, the operator lowers the bucket while simultaneously retracting the dipper handle during the loading cycle. In the time interval from 0 to 8 s, the variables (θ_3) and (d_1) remain constant, at values of 45° and 9 m, respectively.

When the shovel approaches the central position of the working face, the operator begins lowering the bucket and retracting the cylinder to close the bucket gate within the period from 8 to 13 s.

During this period, (θ_3) varies from 45° to –30°, while the dipper handle retracts from 9 to 4 m. In the subsequent loading cycle, the speed commands set by the position references of the hoist and crowd joysticks generate a simultaneous increase in (θ_3) and displacement (d_1), resulting in an upward parabolic trajectory of the bucket.

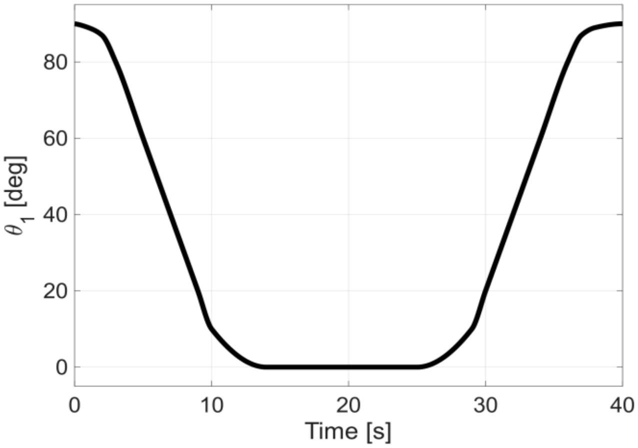

Fig. 9 Swing angular position (Plotted using MATLAB R2025a)

At the end of the loading cycle, (θ_3) returns to its initial value of 45°, the cylinder reaches a maximum extension of 9.5 m, and then retracts to 9 m as the bucket moves away from the working face.

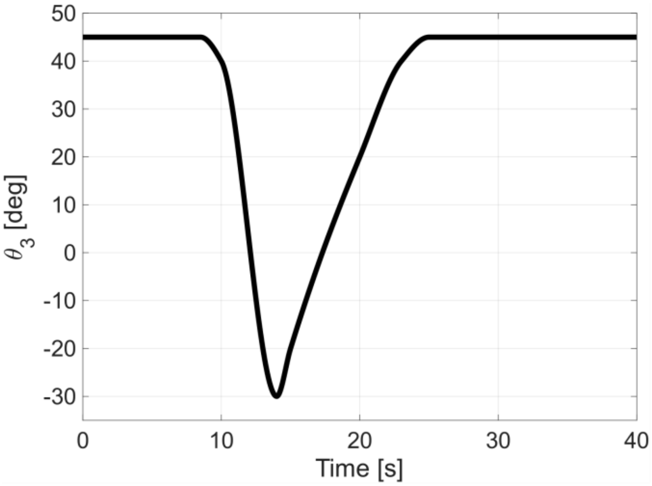

Fig. 10 Hoist angular position (Plotted using MATLAB R2025a)

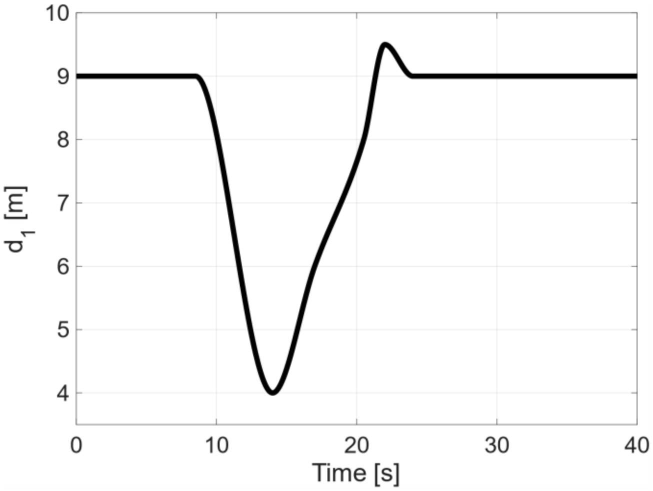

Fig. 11 Crowd displacement (Plotted using MATLAB R2025a)

7. Analysis of Simulated and Field-Recorded Torque Results

As indicated in [16], the most relevant variable influencing power requirements throughout the duty cycle of an electric rope shovel is the torque required during the excavation phase. This torque depends on several variables that exhibit random behavior, making its modeling very challenging.

Considering these indeterminate factors, the most suitable approach to achieving a realistic modeling of excavation torque is to evaluate a large set of field records related to power, torque, and speed and to establish correlations among them. In the present study, a representative set of field records was used. The components of excavation torque were derived from these records, which were extracted from data collected across different types of working faces.

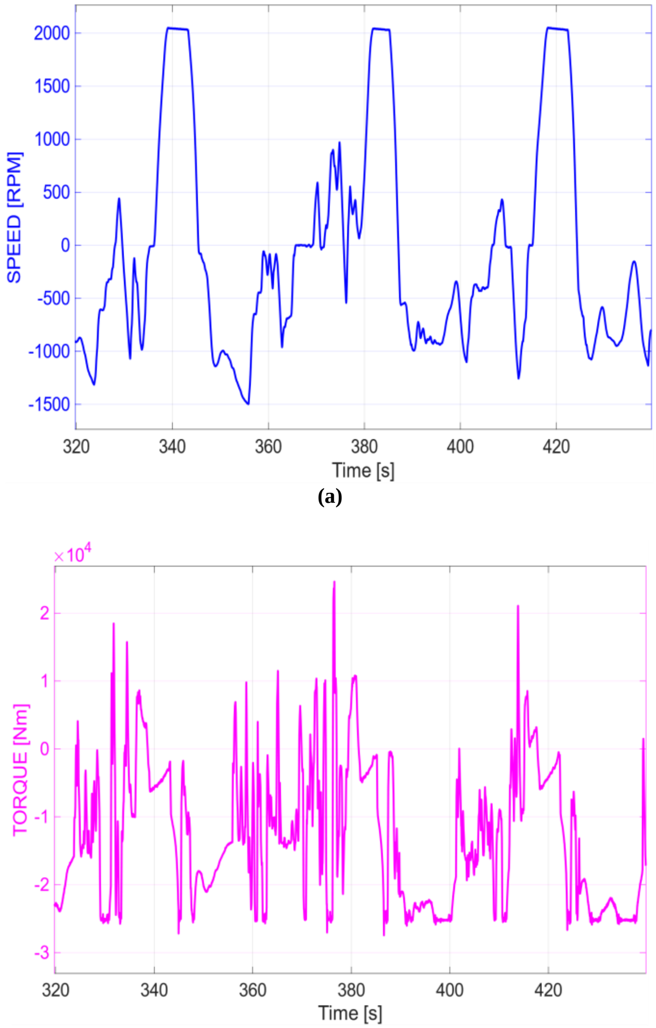

(a)

(b)

Fig. 12 Torque and speed developed by the hoist motor during a load cycle: (a) Speed of the hoist motor, and (b) Torque of the hoist motor (plotted using MATLAB R2025a).

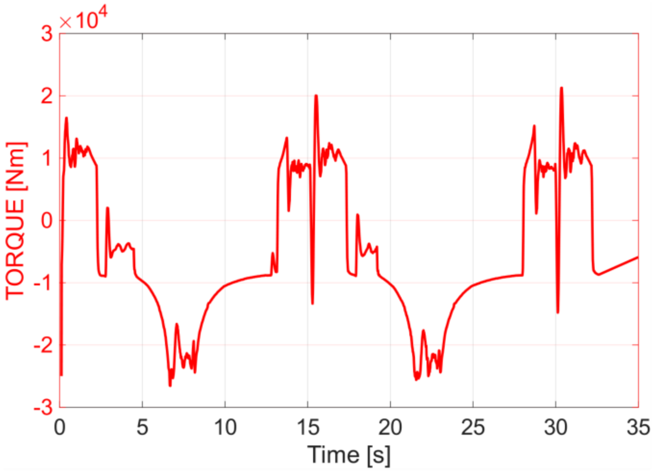

Fig. 13 Hoist motor torque simulation (Plotted using MATLAB R2025a)

7.1. Evaluation of the Signal during Hoist Motion

Figure 12 illustrates the relationship between the torque (pink) and speed (blue) developed by the hoist motor during the truck loading phase. This figure was generated through the processing of field data. The loading phase is divided into three cycles, each lasting approximately 40 seconds.

As shown in Figure 12, at the beginning of each loading cycle, when the shovel operator starts lifting the bucket, there is a noticeable increase in speed accompanied by a significant rise in torque. Table 1 records the three maximum and minimum torque values for each cycle, which enables comparison with the simulated results.

Figure 13 presents the simulated torque for three loading cycles, in which certain variables in the dynamic equation (57) were adjusted to replicate the conditions under which the field data were collected. Similarly, Table 1 lists the three maximum and minimum simulated torque values for each cycle.

By comparing the torque records in Table 1, it can be observed that the simulated maximum and minimum values fall within an acceptable range relative to the actual records. This deviation may be attributed to the use of estimated center of mass variables in the dynamic model, as well as potential differences in material resistance.

7.2. Evaluation of the Signal during Crowd Motion

Figure 14 shows the relationship between the torque (pink) and speed (blue) developed by the crowd motor, obtained from field records.

Table 1. Comparative analysis of hoist motor torque: field records and simulation results during the loading cycle

Toque (Nm)	1.° cycle	2.° cycle	3.° cycle
Max. Rec	18,388	24,636	21,072
Max. Sim	16,455	20,042	21,272
Min. Rec	-27,084	-27,458	-26,666
Min. Sim	-24,986	-26,510	-25,590

The torque behavior in this motion differs from that observed in the hoisting motion. As seen in Figure 14, the speed signal exhibits constant variations, which are due to the operator continuously extending the dipper handle to load the bucket fully. As in the previous case, three loading cycles were considered for the evaluation of the crowd torque.

Table 2. Comparative analysis of crowd motor torque: field records and simulation results during the loading cycle.

Toque (Nm)	1.° cycle	2.° cycle	3.° cycle
Max. Rec	7,682	7,704	7664
Max. Sim	6,450	6,009	5,662
Min. Rec	-520	-1,328	-1,921
Min. Sim	-2,261	-2,249	-2,217

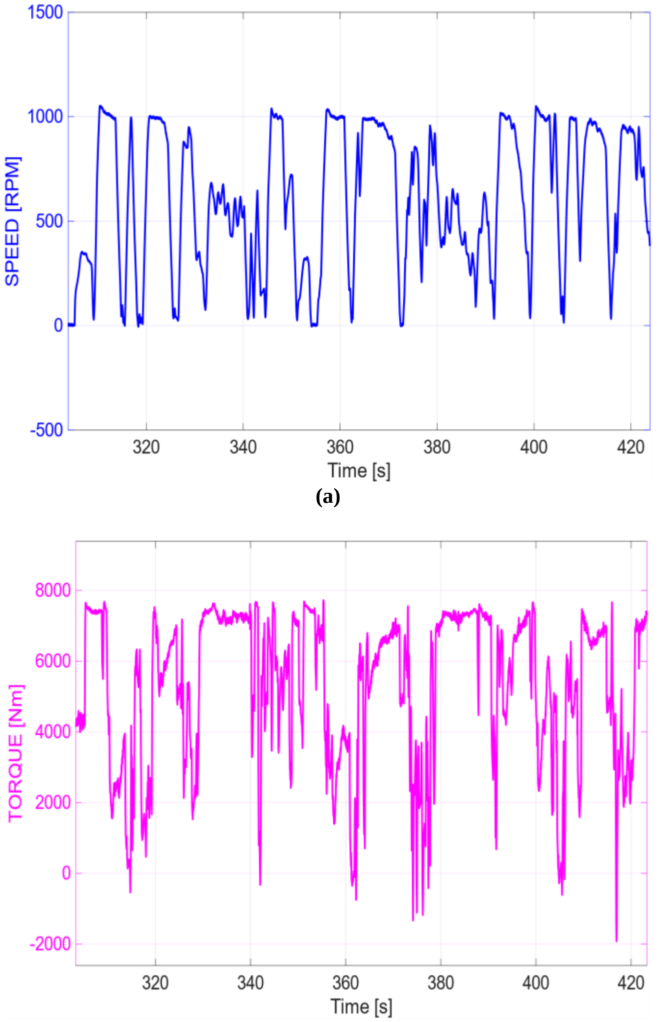

(a)

(b)

Fig. 14 Torque and speed developed by the crowd motor during a load cycle: (a) Speed of the crowd motor, and (b) Torque of the crowd motor (plotted using MATLAB R2025a).

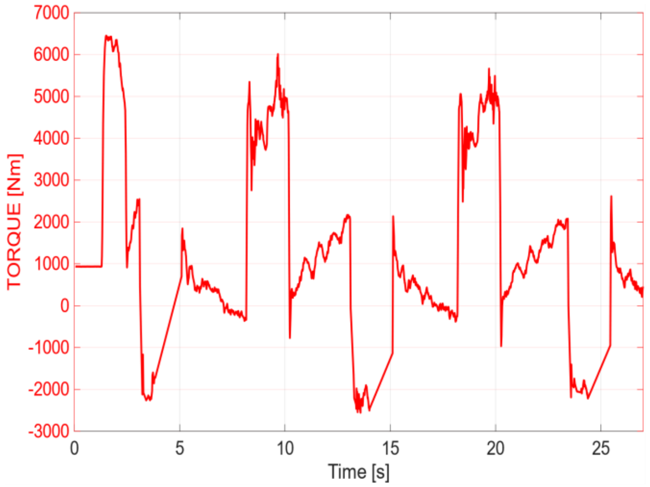

Fig. 15 Crowd motor torque simulation digging torque (Plotted using MATLAB R2025a)

Figure 15 presents the result of the simulated crowd torque, obtained using Equation (59). Similarly, the maximum and minimum torque values for each cycle were recorded in order to compare them with the field-measured torques shown in Table 2.

The only significant difference is observed in the first cycle, where the simulated torque is four times higher than the measured value; however, this case can be considered isolated, as the remaining values fall within an acceptable range.

7.3. Analysis of Regeneration and Consumption Power

As illustrated in Figure 6, all Active Front Ends (AFEs) are interconnected via the DC bus, enabling the energy regenerated on this bus to be redistributed among the motor inverters.

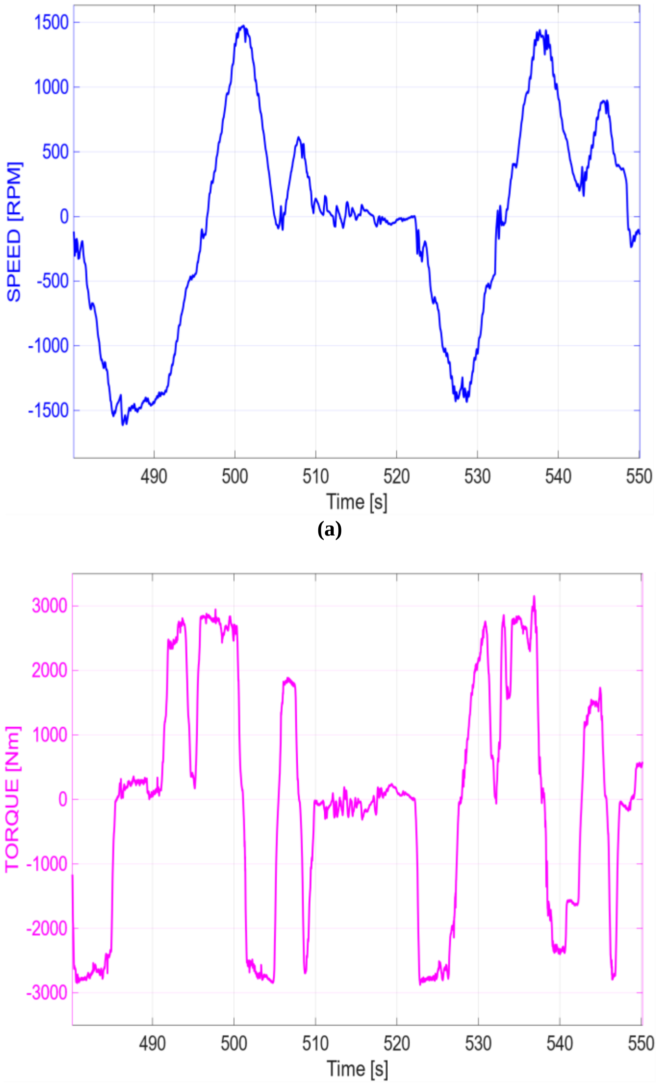

(a)

(b)

Fig. 16 Torque and speed developed by the swing motor during a load cycle: (a) Speed of the swing motor, and (b) Torque of the swing motor (plotted using MATLAB R2025a).

When all motors collectively produce net regenerative energy, this excess energy is returned to the Alternating Current (AC) network through the AFEs. Regeneration predominantly occurs during deceleration events, lowering of the dipper handle, and complete stoppage of the electric rope shovels. The developed mechanical model enables the determination of specific variable values during the excavation stage. This approach allows the simulation of the forces involved in the hoist and crowd motions and, consequently, the interpretation of their behavior with respect to the torque developed by the swing, hoist, and crowd motors. Figure 16 presents two signals: the pink signal represents the torque developed by the two swing motors, while the blue signal corresponds to the speed, which permits interpretation of the swing direction controlled by the shovel operator. In the swing motion, the power signals, as illustrated in Figure 17, display a pattern characterized by increased electrical energy demand from the grid during acceleration phases, followed by energy regeneration during deceleration phases. This phenomenon results in notably low effective energy consumption throughout one cycle, highlighting the advantage of regeneration during the swing motion.

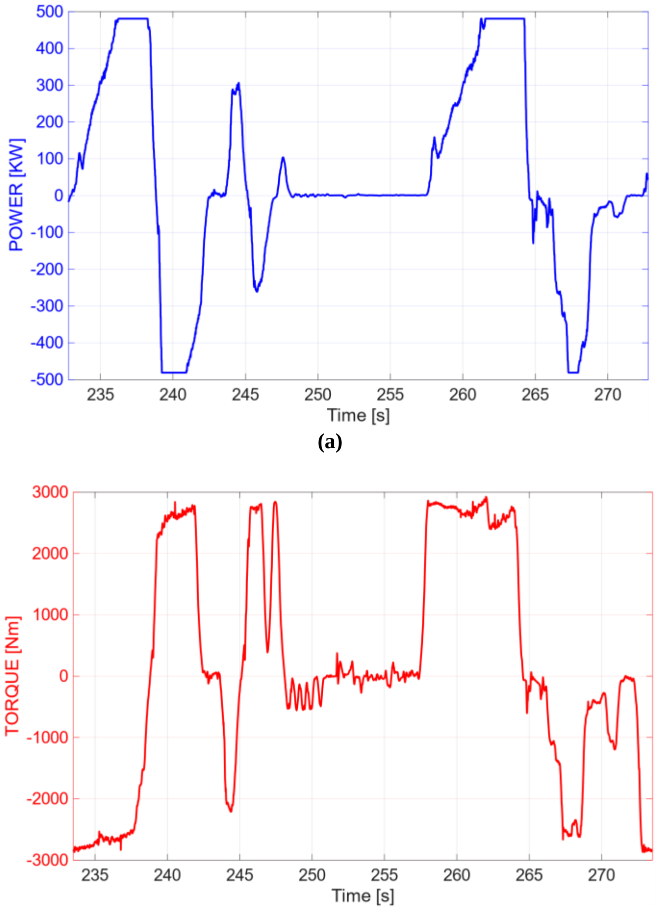

(a)

(b)

Fig. 17 Power and torque developed by the swing motor during a load cycle: (a) Power of the swing motor, and (b) Torque of the swing motor (plotted using MATLAB R2025a).

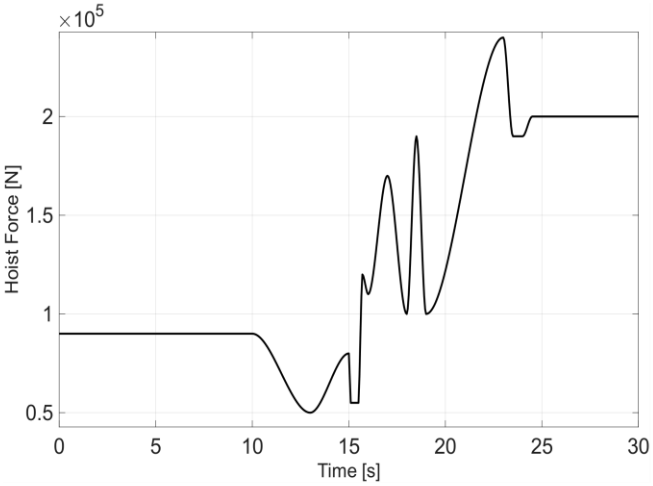

Fig. 18 Hoist force (Plotted using MATLAB R2025a)

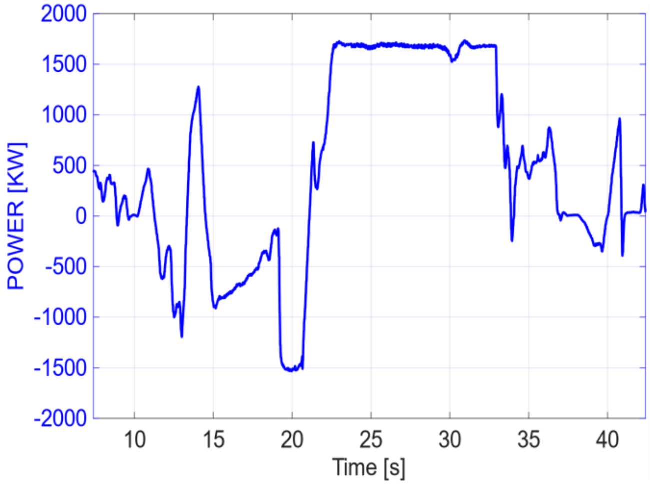

Fig. 19 Hoist active power (Plotted using MATLAB R2025a)

When the operator reaches the final position, a reverse motion is performed to position the dipper above the truck for unloading. During this braking action, a high torque peak is generated. Variables related to the hoist motion are presented in Figure 18, which shows the hoist force (F_H) exerted by the hoist cable to lift the dipper. Figure 19 identifies a regenerative power phenomenon during the dipper's descent, leading to a significant power demand during excavation.

Finally, Figure 20 presents the variables associated with the crowd motion. The graph showing the retraction and extension forces reveals that when retraction is performed under load, a significant increase in force occurs. For the crowd motion, the power curve shown in Figure 21 indicates that there are only brief periods in which regeneration takes place, while power is predominantly manifested as effective consumption during the excavation phase.

8. Analysis and Discussion of Results

The analysis of the results obtained in the hoist and crowd motor torque simulations was performed using a large amount of data obtained from field records taken while the electric shovel was loading trucks. These records helped us simulate real-world work situations, such as the hardness of the workface, the time it takes for trucks to position themselves for loading, operator experience, good and bad operating practices, and truck loading time.

The results presented in Tables 1 and 2 demonstrate a clear similarity between the torque values obtained from field measurements and those derived from the simulation for the hoist and thrust motors during loading cycles. This validates the efficiency of the developed model, demonstrating that the operational behavior of an electric shovel can be reliably replicated under different working conditions. It should be clarified that there are still different variables that make the modeling less than ideal, since variables such as operator experience cannot be replicated. However, improvements can be made in operating practices to avoid damaging the different components of the electric shovel.

In both cases, most of the simulated maximum and minimum values fall within an acceptable range compared to the field records, indicating that the dynamic model employed is capable of replicating the loading cycle behavior under operational conditions. However, some specific discrepancies were observed, particularly in the first crowd cycle, which may be related to variations in material properties or the model's sensitivity to specific initial conditions, as also discussed in [16].

Another relevant aspect to consider, in comparison with the description in [16], is that in that study, the crowd simulations are based on a mechanical system similar to the hoisting mechanism. In contrast, the model developed in this article features a significantly different crowd system, as the movement of the dipper handle is accomplished through a hydraulic system. As a result, the speed of the crowd motor is always positive, leading to a behavior that differs from what is observed in [16].

It should be noted that this analysis evaluates only a single loading cycle, rather than the complete truck loading phase, to facilitate comparison with the results presented in [16]. Once the moments of energy regeneration in the crowd, hoist, and swing motions were identified, the peaks of consumed and regenerated power for each motion during the loading cycle were recorded in Table 3.

Based on these power values, it was possible to calculate both the energy consumed and the energy generated within the corresponding time intervals. Using MATLAB tools, the energy associated with each motion was obtained, and the regeneration percentages were found to be similar to those reported in [16], which validates the reliability of the developed model.

Table 3. Percentage of regenerated energy (E_{reg}) relative to consumed energy (E_{con}) during the Loading Cycle

Motor	P_{con} (kW)	P_{reg} (kW)	E_{con} (MJ)	E_{reg} (MJ)	%
Swing	480.9	461.8	1.903	1.345	70.7%
Hoist	1734	1529	19.15	5.117	26.7%
Crowd	484.5	72.75	2.510	0.031	1.24%
Total	2699.4	2063.5	23.563	6.493	27.5%

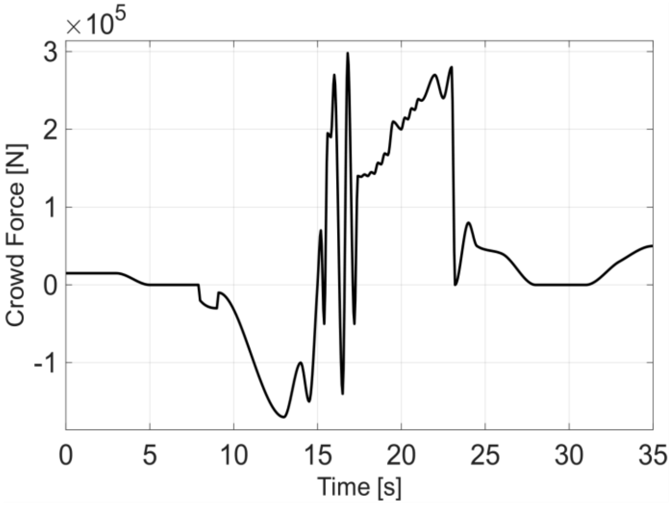

Fig. 20 Crowd force (Plotted using MATLAB R2025a)

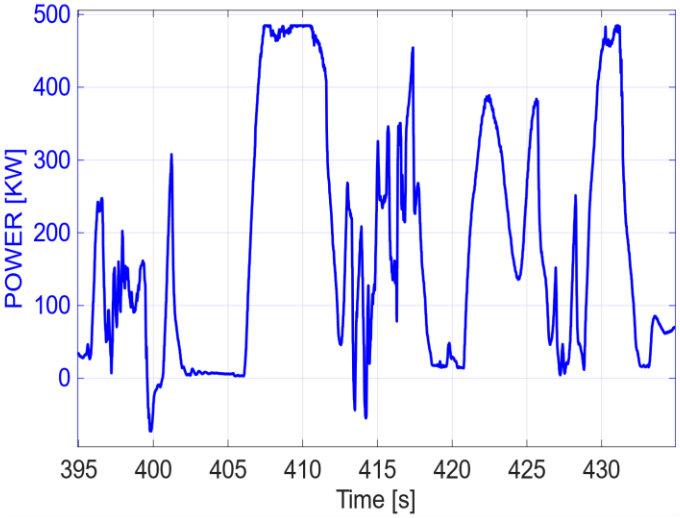

Fig. 21 Crowd active power (Plotted using MATLAB R2025a)

Future studies should get the real values of the center of mass and inertia of the electric shovel parts, as these parameters would make the simulations more accurate and help identify important operating conditions to improve predictive models and use them in more situations.

9. Conclusion

The developed kinematic and dynamic modeling proves to be highly efficient for describing and understanding the equipment's movements during the truck loading cycle. This model enables the simulation of motions to predict the behavior of specific components and to identify possible solutions to conditions that may arise during equipment operation.

The results obtained demonstrate a 27.5% energy savings achieved. Furthermore, this evaluation validates that the integrated model developed for the electric rope shovels constitutes an effective tool for analyzing all relevant mechanical and electrical variables in relation to the operator's commands and the excavation requirements of the working face. This model can be used to assess the effectiveness of the blasting design by extracting the components of the excavation torque and providing operational recommendations to the equipment operator.

The analysis of energy regeneration demonstrates that, by using variable speed drives (VSDs) with regenerative capability, it is possible to quantify the energy recovery during the truck loading cycle. Therefore, if continuous field records are made, energy consumption trends can be obtained under different conditions, allowing for the estimation of energy consumption and operational costs.

The percentages of regenerated energy in a single loading cycle (swing: 70.7%, hoist: 26.7%, crowd: 1.24%) are highly satisfactory, as they contribute to more efficient energy utilization, thereby reducing operational expenses without affecting productivity.

The differences observed in certain cycles, particularly in the first crowd cycle, highlight the importance of further experimental characterization of material properties and the identification of critical operational conditions to further improve the accuracy of predictive models.

Electric rope shovels are among the most important pieces of equipment in open-pit mining; therefore, applications that help improve their availability will have a direct impact on the productivity and overall development of the mining operation.

Acknowledgment

The authors would like to thank the Universidad Nacional de San Agustín (UNSA) and Dr. Fernando from the Universidade Federal de Alagoas (UFAL) for the support provided during the development of this work. We also extend our gratitude to the colleagues who offered valuable comments and recommendations during the preparation of this manuscript.

References

[1] Bud Fox, Leslie Stephen Jennings, and Albert Y.H. Zomaya, "On the Modelling of Actuator Dynamics and the Computation of Prescribed Trajectories," *Computers and Structures*, vol. 80, no. 7-8, pp. 605-614, 2002. [CrossRef] [Google Scholar] [Publisher Link]

[2] Hongjin Wu, "*Modelling and Simulation of Electric Mining Shovels*," M.Sc. Thesis, McGill University, Quebec, Canadá, 1995. [Google Scholar] [Publisher Link]

[3] Minchang Sung, and Youngjin Choi, "Algorithmic Modified Denavit-Hartenberg Modeling for Robotic Manipulators using Line Geometry," *Applied Sciences*, vol. 15, no. 9, pp. 1-29, 2025. [CrossRef] [Google Scholar] [Publisher Link]

[4] Samuel Frimpong, Yafei Hu, and Kwame Awuah-Offei, "Mechanics of Cable Shovel-Formation Interactions in Surface Mining Excavations," *Journal of Terramechanics*, vol. 42, no. 1, pp. 15-33, 2005. [CrossRef] [Google Scholar] [Publisher Link]

[5] Jisong Ding, Huafeng Ding, and Wenjian Yang, "Dynamic Modeling of a Novel Multi-Loop Multi-Body Mechanism of Face-Shovel Excavator," *Chinese Journal of Mechanical Engineering*, vol. 38, no. 1, pp. 1-17, 2025. [CrossRef] [Google Scholar] [Publisher Link]

[6] Jose Rodriguez et al., "Operating Experience of Shovel Drives for Mining Applications," *IEEE Transactions on Industry Applications*, vol. 40, no. 2, pp. 664-671, 2004. [CrossRef] [Google Scholar] [Publisher Link]

[7] Premananda Pany, "Design and Control of Active Front End Converters for Traction Application," *International Journal of Scientific Engineering and Research*, vol. 6, no. 6, pp. 70-74, 2018. [Google Scholar] [Publisher Link]

[8] Wei Zhang et al., "Research on Regenerative Braking of Pure Electric Mining Dump Truck," *World Electric Vehicle Journal*, vol. 10, no. 2, pp. 1-17, 2019. [CrossRef] [Google Scholar] [Publisher Link]

[9] Juan S. Gómez et al., "An Overview of Microgrids Challenges in the Mining Industry," *IEEE Access*, vol. 8, pp. 191378-191393, 2020. [CrossRef] [Google Scholar] [Publisher Link]

[10] Hao Feng et al., "Multi-Objective Time-Energy-Impact Optimization for Robotic Excavator Trajectory Planning," *Automation in Construction*, vol. 156, 2023. [CrossRef] [Google Scholar] [Publisher Link]

[11] Karol Cieślik et al., "The Influence of the Operator's Perception on the Energy Demand for a Hydraulic Manipulator with a Large Working Area," *Applied Sciences*, vol. 14, no. 5, pp. 1-19, 2024. [CrossRef] [Google Scholar] [Publisher Link]

[12] Frank A. Bender et al., "Predictive Operator Modeling for Virtual Prototyping of Hydraulic Excavators," *Automation in Construction*, vol. 84, pp. 133-145, 2017. [CrossRef] [Google Scholar] [Publisher Link]

[13] Guodong Liang et al., "Dynamic Modeling and Analysis of Loader Working Mechanism Considering Cooperative Motion with the Vehicle Body," *Machines*, vol. 11, no. 1, pp. 1-27, 2022. [CrossRef] [Google Scholar] [Publisher Link]

[14] John J. Craig, *Introduction to Robotics: Mechanics and Control*, 3rd ed., Pearson Education India, 2009. [Google Scholar]

[15] Antonio Barrientos et al., *Fundamentals of Robotics*, 2nd ed., McGraw Hill, 2007. [Google Scholar]

[16] Matías Valenzuela Guzmán, and M. Aníbal Valenzuela, "Integrated Mechanical-Electrical Modeling of an AC Electric Mining Shovel and Evaluation of Power Requirements During a Truck Loading Cycle," *IEEE Transactions on Industry Applications*, vol. 51, no. 3, pp. 2590-2599, 2015. [CrossRef] [Google Scholar] [Publisher Link]

[17] Abdolrasul Rasuli, Shahram Tafazoli, and William G. Dunford, "Dynamic Modeling, Parameter Identification, and Payload Estimation of Mining Cable Shovels," *2014 IEEE Industry Application Society Annual Meeting*, Vancouver, BC, Canada, pp. 1-9, 2014. [CrossRef] [Google Scholar] [Publisher Link]

[18] Peter Corke, "Robot Manipulator Capability in MATLAB: A Tutorial on using the Robotics System Toolbox [Tutorial]," *IEEE Robotics and Automation Magazine*, vol. 24, no. 3, pp. 165-166, 2017. [CrossRef] [Google Scholar] [Publisher Link]

[19] Peter Corke, Witold Jachimczyk, and Remo Pillat, *Robotics, Vision and Control: Fundamental Algorithms in MATLAB*, 3rd ed., Springer Cham, 2023. [CrossRef] [Google Scholar] [Publisher Link]

[20] Joseph E. Shigley, Charles R. Mischke, and Richard G. Budynas, *Mechanical Engineering Design*, New York: Mc Graw-Hill, 2004. [Google Scholar]

[21] G.M. Brown, B.J. Elbacher, and Walter G. Koellner, "Increased Productivity with AC Drives for Mining Excavators and Haul Trucks," *Conference Record of the 2000 IEEE Industry Applications Conference. Thirty-Fifth IAS Annual Meeting and World Conference on Industrial Applications of Electrical Energy (Cat. No.00CH37129)*, Rome, Italy, vol. 1, pp. P28-P37, 2000. [CrossRef] [Google Scholar] [Publisher Link]

[22] Joy Mazumdar, "Regeneration Energy Management in AC Mining Drives for Providing Control Power," *2009 IEEE Industry Applications Society Annual Meeting*, Houston, TX, USA, pp. 1-5, 2009. [CrossRef] [Google Scholar] [Publisher Link]

Appendix 1: Simulation of the Kinematic System of an Electric Rope Shovel

```
startup_rvc;
%%Primeramente referenciamos nuestro marco {0} de referencia inicial que en
%%este caso es el centro de giro de la Pala Eléctrica
R = eye(3)
```

```
t = [0 0 0]'
T = [R t; 0 0 0 1]
trplot(T,'frame','T0','color','b');
pause
%%Para el marco de referencia {1} se esta tomando un giro de 90° que
%%es el necesario para posicionarse para cargar un camión minero
T1 = trotz(pi/2)
hold on;
tranimate(T1,'frame','T1','color','r');
pause
%%Para el marco de referencia {2} tiene que haber un desplazamiento
%%desde el pin central hacia el pie de boom y la inclinación del boom
%%respecto al piso es de 45°
R1 = roty(-pi/4)*rotx(pi/2)
t = [0.69 0 0]'
T2 = [R1 t; 0 0 0 1]
hold on;
tranimate(T2,'frame','T2','color','g');
pause
%%Para el marco de referencia {3} se tiene un desplazamiento desde el
%%pie de boom hasta el Shipper Shaft
T3 = T2*transl(0.9,0,0)*trotz(pi/4)
hold on;
tranimate(T3,'frame','T3','color','c');
pause
%%Para el marco de referencia {4}se tiene un desplazamiento la cual nos
%%llevará al medio del saddle block y luego se tendrá que desplazar hacia
%%el pin del Dipper Handle
T4 = T3*transl(0.1,-1.4,0)*trotx(pi/2)
hold on;
tranimate(T4,'frame','T4','color','m');
pause
>> MH_Shovel_Electric
Robotics, Vision & Control: (c) Peter Corke 1992-2019 http://www.petercorke.com
T_1 =
[cos(theta1), -sin(theta1), 0, 0]
[sin(theta1),  cos(theta1), 0, 0]
[          0,            0, 1, 0]
[          0,            0, 0, 1]

T_2 =
[ cos(theta2), sin(theta2),  0, a1]
[           0,           0, -1,  0]
[-sin(theta2), cos(theta2),  0,  0]
[           0,           0,  0,  1]

T_3 =
[cos(theta3), -sin(theta3), 0, a2]
[sin(theta3),  cos(theta3), 0,  0]
```

```
[          0,           0, 1,  0]
[          0,           0, 0,  1]

T_4 =
[1, 0,  0,  a3]
[0, 0, -1, -d1]
[0, 1,  0,   0]
[0, 0,  0,   1]
```

Appendix 2: Simulation of a dynamic system, electric rope shovel

```
% Variables
syms theta1 theta2 theta3 a1 a2 a3 d1 dd1 ddd1 dtheta1 dtheta2 dtheta3 g
syms ddtheta1 ddtheta2 ddtheta3 m1 m2 m3 m41 m42 mload
syms h1 l1 w1 h2 l2 w2 h3 l3 w3 h41 l41 w41 h42 l42 w42 cx2 cy2 cx4
% Inercias
%
Ixx1 = 0.33*m1*(l1^2+h1^2);
Iyy1 = 0.33*m1*(w1^2+h1^2);
Izz1 = 0.33*m1*(l1^2+w1^2);
Ixy1 = 0.25*m1*w1*l1;
Ixz1 = 0.25*m1*h1*w1;
Iyz1 = 0.25*m1*h1*l1;
i1  = [Ixx1 -Ixy1 -Ixz1; -Ixy1 Iyy1 Iyz1; -Ixz1 -Iyz1 Izz1];
%2
Ixx2 = 0.33*m2*(l2^2+h2^2);
Iyy2 = 0.33*m2*(w2^2+h2^2);
Izz2 = 0.33*m2*(l2^2+w2^2);
Ixy2 = 0.25*m2*w2*l2;
Ixz2 = 0.25*m2*h2*w2;
Iyz2 = 0.25*m2*h2*l2;
i2  = [Ixx2 -Ixy2 -Ixz2; -Ixy2 Iyy2 Iyz2; -Ixz2 -Iyz2 Izz2];
%3
Ixx3 = 0.33*m3*(l3^2+h3^2);
Iyy3 = 0.33*m3*(w3^2+h3^2);
Izz3 = 0.33*m3*(l3^2+w3^2);
Ixy3 = 0.25*m3*w3*l3;
Ixz3 = 0.25*m3*h3*w3;
Iyz3 = 0.25*m3*h3*l3;
i3  = [Ixx3 -Ixy3 -Ixz3; -Ixy3 Iyy3 Iyz3; -Ixz3 -Iyz3 Izz3];
%41
Ixx41 = 0.33*m41*(l41^2+h41^2);
Iyy41 = 0.33*m41*(w41^2+h41^2);
Izz41 = 0.33*m41*(l41^2+w41^2);
Ixy41 = 0.25*m41*w41*l41;
Ixz41 = 0.25*m41*h41*w41;
Iyz41 = 0.25*m41*h41*l41;
i41  = [Ixx41 -Ixy41 -Ixz41; -Ixy41 Iyy41 Iyz41; -Ixz41 -Iyz41 Izz41];
%42
Ixx42 = 0.33*m42*(l42^2+h42^2);
```

```
Iyy42 = 0.33*m42*(w42^2+h42^2);
Izz42 = 0.33*m42*(l42^2+w42^2);
Ixy42 = 0.25*m42*w42*l42;
Ixz42 = 0.25*m42*h42*w42;
Iyz42 = 0.25*m42*h42*l42;
i42  = [Ixx42 -Ixy42 -Ixz42; -Ixy42 Iyy42 Iyz42; -Ixz42 -Iyz42 Izz42];
% Matriz de transformación homogénea del marco de referencia {1} respecto
% al marco de referencia {0}
R_1  = rotz(theta1);
p_1  = [0;0;0];
T_1  = [R_1 p_1; 0 0 0 1]
% Velocidades
V_00 = [0;0;0];
W_00 = [0;0;0];
W_11 = R_1*[0;0;0] + dtheta1*[0;0;1]
W_P1 = cross(W_00,p_1);
V_11 = R_1*([0;0;0] + W_P1)
% Aceleraciones
DV_00 = [0;g;0];
DW_00 = [0;0;0];
A_1   = dtheta1*[0;0;1];
A_2   = R_1*W_00;
A1    = cross(A_2,A_1);
DW_11 = R_1*DW_00 + A1 + ddtheta1*[0;0;1]
A2    = cross(W_00,p_1);
A3    = cross(W_00,A2);
DV_11 = R_1*(A2 + A3 + DV_00)
% Centro de Masa 1
PC1   = [0;0;0];
A4    = W_11 + PC1;
DVC_11 = cross(DW_11,PC1) + cross(W_11,A4) + DV_11
%%
% Matriz de transformación homogénea del marco de referencia {2} respecto
% al marco de referencia {1}
Rx_2 = rotx(pi/2);
MR   = round(Rx_2);
R_2  = roty(theta2)*MR;
p_2  = [a1;0;0];
T_2  = [R_2 p_2; 0 0 0 1]
% Velocidades
W_22 = R_2*W_11 + dtheta2*[0;0;1]
W_P2 = cross(W_11,p_2);
V_22 = R_2*(V_11 + W_P2)
% Aceleraciones
B_1   = dtheta2*[0;0;1];
B_2   = R_2*W_11;
B1    = cross(B_1,B_2);
DW_22 = R_2*DW_11 + B1 + ddtheta2*[0;0;1]
B2    = cross(W_11,p_2);
```

```
B3    = cross(W_11,B2);
DV_22 = R_2*(B2 + B3 + DV_11)
% Centro de Masa 2
PC2   = [cx2;-cy2;0];
B4    = W_22 + PC2;
DVC_22 = cross(DW_22,PC2) + cross(W_22,B4) + DV_22
%%
% Matriz de transformación homogénea del marco de referencia {3} respecto
% al marco de referencia {2}
R_3  = rotz(theta3);
p_3  = [a2;0;0];
T_3  = [R_3 p_3; 0 0 0 1]
% Velocidad
W_33 = R_3*W_22 + dtheta3 * [0;0;1]
W_P3 = cross(W_22, p_3);
V_33 = R_3*(V_22 + W_P3)
% Aceleraciones
C_1   = dtheta3*[0;0;1];
C_2   = R_3*W_22;
C1    = cross(C_1,C_2);
DW_33 = R_3*DW_22 + C1 + ddtheta3*[0;0;1]
C2    = cross(W_22,p_3);
C3    = cross(W_22,C2);
DV_33 = R_3*(C2 + C3 + DV_22)
% Centro de Masa 3
PC3   = [a3;0;0];
C4    = W_33 + PC3;
DVC_33= cross(DW_33,PC3) + cross(W_33,C4) + DV_33
%%
% Matriz de transformación homogénea del marco de referencia {4} respecto
% al marco de referencia {3}
Rx_4 = rotx(pi/2);
MR_4   = round(Rx_4);
R_4  = MR_4;
p_4  = [a3;-d1;0];
T_4  = [R_4 p_4; 0 0 0 1]
% Velocidades
W_44 = R_4*W_33
W_P4 = cross(W_33,p_4);
V_44 = R_4*(V_33 + W_P4) - dd1*[0;0;1]
% Aceleraciones
DW_44 = R_3*W_33
D0    = cross(DW_33,p_4);
D1    = cross(W_33,p_4);
D2    = cross(W_33,D1);
D3    = dd1*[0;0;1];
D4    = cross(W_33,D3);
DV_44 = R_4*(D0 + D2 + DV_33) + 2*D4 + ddd1*[0;0;1]
% Centro de Masa 41
```

```
PC41   = [0;0;-0.5*d1];
D5     = W_44 + PC41;
DVC_41 = cross(DW_44,PC41) + cross(W_44,D5) + DV_44
% Centro de Masa 41
PC42   = [cx4;0;0];
D6     = W_44 + PC42;
DVC_42 = cross(DW_44,PC42) + cross(W_44,D6) + DV_44
%%
% Fuerzas respecto al centro de masa
F_1  = m1*DVC_11;
F_2  = m2*DVC_22;
F_3  = m3*DVC_33;
F_41 = m41*DVC_41;
F_42 = (m42 + mload)*DVC_42;
%%
% momentos de torque
N_A1 = i1*W_11;
N_1  = i1*DW_11 + cross(W_11,N_A1);

N_B1 = i2*W_22;
N_2  = i2*DW_22 + cross(W_22,N_B1);

N_C1 = i3*W_33;
N_3  = i3*DW_33 + cross(W_33,N_C1);

N_D41 = i41*W_44;
N_41  = i41*DW_44 + cross(W_44,N_D41);

N_D42 = i42*W_44;
N_42  = i42*DW_44 + cross(W_44,N_D42);
%%
% Total de fuerzas y momento de torque que actuan en cada eslabon
NRx_2 = rotx(-pi/2);
NMR   = round(NRx_2);
NR_2  = roty(-theta2)*MR;
NR_3  = rotz(-theta3);
NRx_4 = rotx(-pi/2);
NMR_4 = round(NRx_4);
NR_4  = NMR_4;
f4  = F_41 + F_42;
f3  = F_3 + NR_4*f4;
f2  = F_2 + NR_3*f3;
f1  = F_1 + NR_2*f2;
n4  = (N_41 + N_42) + cross(PC41,F_41) + cross(PC42,F_42);
CN3 = NR_4*f4;
n3  = N_3 + NR_4*n4 + cross(PC3,F_3) + cross(PC3,CN3);
CN2 = NR_3*f3;
n2  = N_2 + NR_3*n3 + cross(PC2,F_2) + cross(PC2,CN2);
CN1 = NR_2*f2;
```

```
n1  = N_1 + NR_2*n2 + cross(PC1,F_1) + cross(PC1,CN1);
%torques totales
t1 = n1'*[0 0 1]'
t2 = n2'*[0 0 1]'
t3 = n3'*[0 0 1]'
t4 = f4'*[0 0 1]'
```

Appendix 3: Simulation of the energy consumed in a loading cycle.

```
% LEER BASE DE DATOS
%
data = readtable('HOIST_V1.xlsx','Sheet','JUN6 MONV1');
%swing (intervalo T: 232.931-238.814 & 238.814-242.624)
t = data{:,11};      % Tiempo (en segundos)
P_kW = data{:,12};   % Potencia en kW
% Convertir a Watts
P = P_kW * 1000;
%
% SELECCIONAR INTERVALO DE TIEMPO
%
fprintf('Intervalo disponible: %.3f s  hasta  %.3f s\n', t(1), t(end));
t_inicio = input('Ingrese el tiempo inicial del intervalo: ');
t_final  = input('Ingrese el tiempo final del intervalo: ');
% Validación
if t_inicio >= t_final
    error('El tiempo inicial debe ser menor al tiempo final.');
end
% Encontrar índices que están dentro del intervalo
indices = find(t >= t_inicio & t <= t_final);
% Extraer el intervalo
t_int = t(indices);
P_int = P(indices);
%
% CALCULAR ENERGÍA EN JOULES
%
E_J = trapz(t_int, P_int);
fprintf('\n=========================================\n');
fprintf('Tiempo inicial: %.3f s\n', t_inicio);
fprintf('Tiempo final:    %.3f s\n', t_final);
fprintf('Energía total en ese intervalo: %.3f Joules\n', E_J);
fprintf('=========================================\n');
%%
% GRAFICAR INTERVALO SELECCIONADO
%
figure;
hold on; grid on;
plot(t, P, ‘Color’, [0.7 0.7 0.7], ‘DisplayName’, ‘Potencia total’);
plot(t_int, P_int, ‘LineWidth’, 2, ‘Color’, [1 0 1], ...
     'DisplayName', 'Intervalo seleccionado');
xlabel('Tiempo (s)');
```

```
ylabel('Potencia (W)');
title('Cálculo de Energía en Intervalo de Tiempo');
legend('show');
%%
data = readtable('HOIST_V1.xlsx','Sheet','JUN4 MONV1');
%swing (intervalo T: 21.0957 -- 33.8708 & 14.526--21.096
t = data{:,11};      % Tiempo (en segundos)
P_kW = data{:,12};   % Potencia en kW
% Convertir a Watts
P = P_kW * 1000;
%
% SELECCIONAR INTERVALO DE TIEMPO
%
fprintf('Intervalo disponible: %.3f s  hasta  %.3f s\n', t(1), t(end));
t_inicio = input('Ingrese el tiempo inicial del intervalo: ');
t_final  = input('Ingrese el tiempo final del intervalo: ');
% Validación
if t_inicio >= t_final
    error('El tiempo inicial debe ser menor al tiempo final.');
end
% Encontrar índices que están dentro del intervalo
indices = find(t >= t_inicio & t <= t_final);
% Extraer el intervalo
t_int = t(indices);
P_int = P(indices);
%
% CALCULAR ENERGÍA EN JOULES
%
E_J = trapz(t_int, P_int);
fprintf('\n=====================================\n');
fprintf('Tiempo inicial: %.3f s\n', t_inicio);
fprintf('Tiempo final:    %.3f s\n', t_final);
fprintf('Energía total en ese intervalo: %.3f Joules\n', E_J);
fprintf('=====================================\n');
%%
data = readtable('HOIST_V1.xlsx','Sheet','JUN5 MONV1');
%swing (intervalo T: 406.083 s -- 412.457 & 399.598--400.571
t = data{:,10};      % Tiempo (en segundos)
P_kW = data{:,11};   % Potencia en kW
% Convertir a Watts
P = P_kW * 1000;
%
% SELECCIONAR INTERVALO DE TIEMPO
%
fprintf('Intervalo disponible: %.3f s  hasta  %.3f s\n', t(1), t(end));
t_inicio = input('Ingrese el tiempo inicial del intervalo: ');
t_final  = input('Ingrese el tiempo final del intervalo: ');
% Validación
if t_inicio >= t_final
```

```
    error('El tiempo inicial debe ser menor al tiempo final.');
end
% Encontrar índices que están dentro del intervalo
indices = find(t >= t_inicio & t <= t_final);
% Extraer el intervalo
t_int = t(indices);
P_int = P(indices);
% CALCULAR ENERGÍA EN JOULES
%
E_J = trapz(t_int, P_int);
fprintf('\n====================================\n');
fprintf('Tiempo inicial: %.3f s\n', t_inicio);
fprintf('Tiempo final:    %.3f s\n', t_final);
fprintf('Energía total en ese intervalo: %.3f Joules\n', E_J);
fprintf('====================================\n');
```